# Examining Impacts of Mass-Diameter (m-D) and Area-Diameter (A-D) Relationships of Ice Particles on Retrievals of Effective Radius and Ice Water Content from Radar and Lidar Measurements

Seung-Hee Ham[1], Seiji Kato[2], and Fred G. Rose[1]

[1]Science Systems and Applications Inc. (SSAI), Hampton, Virginia, USA

[2]NASA Langley Research Center, Hampton, Virginia, USA

# Abstract

Mass-diameter (m-D) and projected area-diameter (A-D) relations are often used to describe the shape of nonspherical ice particles. This study analytically investigates how retrieved effective radius ($r_{eff}$) and ice water content (IWC) from radar and lidar measurements depend on the assumption of m-D [$m(D) = a\,D^b$] and A-D [$A(D) = \gamma\,D^\delta$] relationships. We assume that unattenuated reflectivity factor ($Z$) and visible extinction coefficient ($k_{ext}$) by cloud particles are available from the radar and lidar measurements, respectively. A sensitivity test shows that $r_{eff}$ increases with increasing $a$, decreasing $b$, decreasing $\gamma$, and increasing $\delta$. It also shows that a 10% variation of $a$, $b$, $\gamma$, and $\delta$ induces more than a 100% change of $r_{eff}$. In addition, we consider both gamma and lognormal particle size distributions (PSDs), and examine the sensitivity of $r_{eff}$ to the assumption of PSD. It is shown that $r_{eff}$ increases by up to 10% with increasing dispersion ($\mu$) of the gamma PSD by 2, when large ice particles are predominant. Moreover, $r_{eff}$ decreases by up to 20% with increasing the width parameter ($\omega$) of the lognormal PSD by 0.1. We also derive an analytic conversion equation between two effective radii when different particle shapes and PSD assumptions are used. When applying the conversion equation to nine types of m-D and A-D relationships, $r_{eff}$ easily changes up to 30%. The proposed $r_{eff}$-convertion method can be used to eliminate the inconsistency of assumptions that made in a cloud retrieval algorithm and a forward radiative transfer model.



**Keywords:** Ice particle shape, mass-Diameter (m-D), Area-Diameter (A-D), effective radius, ice water content (IWC), radar, lidar, reflectivity, visible extinction coefficient, particle size distribution (PSD)


**Key points:**

1. Ice particle shape determines m-D and A-D relations, which is used for radar-lidar retrievals.
2. Effective radius is a function of coefficients in m-D and A-D relations.
3. The convertion method of an effective radius is derived when different m-D and A-D are used.

## 1. Introduction

Nonspherical particles have a smaller mass and a projected area than spherical particles for a given maximum diameter (or maximum dimension), *D*. Numerous field campaigns using improved instruments and techniques have measured individual ice particle shapes [e.g., Field et al., 2006, Lawson et al., 2006; McFarquhar et al., 2007; Lawson, 2011; Um et al., 2015], and provided relationships between mass and *D* (m-D), and projected area and *D* (A-D). Ice particle shapes of liquid-topped clouds in temperature between –20°C and –3°C are relatively well-known [Myagkov et al., 2016]. However, for colder temperatures, mass and area of ice particles significantly vary with region, temperature, and cloud type, implying that large uncertainties exist in describing the m-D and A-D relationships.

Space-borne radar and lidar sensors such as Cloud-Aerosol Lidar with Orthogonal Polarization (CALIOP) aboard Cloud-Aerosol Lidar and Infrared Pathfinder Satellite Observations (CALIPSO) [Winker et al., 2003, 2009] and Cloud Profiling Radar (CPR) aboard CloudSat [Stephens et al., 2002, 2008] provide an opportunity of cloud retrievals from combined radar and lidar sensors at a global scale, as shown in Okamoto et al. [2003], Tinel et al. [2005], Delanoë and Hogan [2008, 2010], Stein et al. [2011], and Deng et al. [2010, 2013]. Since the radar and lidar have different sensitivities to cloud optical properties, combining these two active instruments, in principle, brings more detailed and accurate vertical structures of cloud layers than a single active sensor or a passive sensor. However, the radar and lidar retrieval algorithms require an assumption of m-D and A-D relationships, because the radar reflectivity factor is proportional to the mass-squared, and the lidar extinction coefficient is proportional to the projected area of ice particles. Since the m-D and A-D relationships depend on particle shape, retrieved cloud properties differ depending on the assumption of particle shape used for the radar and lidar retrievals.

Several studies have pointed out the importance of the knowledge of particle shape in radar and/or lidar cloud retrievals. Donovan and Van Lammeren [2001] suggested a factor of 3 of differences in retrieved effective radius ($r_{eff}$) due to a particle shape assumption. Hogan et al. [2006a] applied two different particle shapes from Francis et al. [1998] and Mitchell et al. [1996], and found 30% of differences in retrieved $r_{eff}$ and ice water content (IWC). Fontaine et al. [2014] examined impacts of m-D and A-D relationships in determining a reflectivity-IWC (Z-IWC) relationship. Stein et al. [2011] examined a sensitivity of radar-lidar and passive retrieval algorithms to particle shape. Mace and Benson [2017] found 30–200% of differences in retrieving precipitation rate from a Doppler radar depending on ice bulk density, which is predominantly a function of ice particle shape. Other studies also point out importance of particle shape in radar reflectivity forward model. For example, Sato and Okamoto [2006] examined how the radar reflectivity changes with particle shape, and they found 5dB of radar reflectivity differences for $r_{eff} < 100$ μm, and 13 dB for 100 μm $< r_{eff} < 600$ μm. Hammonds et al. [2014] also suggested 4 dB of uncertainties in radar reflectivity simulation depending on mass-dimensional relationship.

When one computes irradiance profiles at a global scale, one might need to use cloud properties such as $r_{eff}$ and optical depth derived from different cloud algorithms because no single retrieval algorithm can provide the properties everywhere all the time. Because the ice $r_{eff}$ particularly depends on the assumption of ice particle shape, one needs to use $r_{eff}$ with a consistent particle shape assumption in the forward radiative transfer model and cloud retrieval. Another option is to develop a relationship to convert the ice $r_{eff}$ derived with a specific particle shape into $r_{eff}$ with a different particle shape assumption for the consistency.

In this study, we analytically derive the relationship between two $r_{eff}$ retrieved from different particle shape assumptions. This differs from earlier studies [e.g., Hogan et al., 2006a; Fontaine et al., 2014; Stein et al., 2011] that examined impacts of particle shape on $r_{eff}$ numerically. We start with an assumption that lidar extinction and radar reflectivity factor are known (or fixed) from lidar and radar observations, respectively. Then $r_{eff}$ and IWC are expressed by coefficients of m-D and A-D relationships. This approach is similar to the one by Donovan and Van Lammeren [2001]. They examined how particle shape assumptions change the relationship between $r_{eff}$ and $r_{eff}'$, where $r_{eff}'$ is defined as the ratio of radar reflectivity to lidar-derived extinction coefficient, hereafter referred as radar-lidar-ratio. In this study, we directly relate $r_{eff}$ to the measured radar-lidar-ratio, instead of using $r_{eff}'$ for various particle shapes. We also use the first derivative of the analytical expression to quantify the sensitivity of $r_{eff}$ to particle shape.

In addition, we examine how well radar and lidar observations can constrain the effective radius, which is a function of particle size distribution (PSD). Generally, the number of unknowns in the PSD is greater than the number of equations that can be set up from observations. Assumptions of one or two parameters of a PSD are often made to reduce the number of unknowns but they introduce an error. We examine the sensitivity of retrieved effective radius to frequently-assumed parameters in the PSD.

Section 2 compares pre-existing m-D and A-D relationships, and Section 3 derives integrated optical properties such as effective radius ($r_{eff}$) and IWC with a gamma PSD. Then uncertainties in retrievals of $r_{eff}$ and IWC are further examined with the derivative of equations of $r_{eff}$ with respect to parameters of m-D and A-D relations. Section 4 uses a lognormal PSD, and compares the results with those from the gamma PSD. Section 5 demonstrates simple applications of this study, a conversion of $r_{eff}$ when different m-D and A-D relationships and/or PSD are used between two radar-lidar algorithms.

## 2. Methodology

### 2.1. Mass-Diameter (m-D) and Area-Diameter (A-D) relationships

Often power laws are used to describe the mass or area distribution of nonspherical ice particles [e.g., Brown and Francis, 1995; Mitchell, 1996; Mitchell et al., 1996; Francis et al., 1998; Heymsfield et al., 2013]:

$$m(D) = aD^{b} \quad , \qquad (1)$$

$$A(D) = \gamma D^{\delta} \quad , \qquad (2)$$

where $m$ is the mass of cloud particles, $A$ is the projected area of cloud particles, and $D$ is the maximum diameter (or the maximum linear dimension of the particle). Unless noted, all variables have centimeter-gram-second (CGS) units throughout this study. Therefore, $D$ is in the unit of cm, $a$ is in the unit of g cm$^{-b}$, $m(D)$ is in gram, $\gamma$ is in the unit of cm$^{2-\delta}$ and $A(D)$ is in cm$^2$.

Table 1 summarizes coefficients $a$, $b$, $\gamma$, and $\delta$ of power laws used in several studies. Brown and Francis [1995] provided a m-D relation for $D \geq 97 \times 10^{-4}$ cm (= 97 μm), while spherical assumption can be used for D < $97 \times 10^{-4}$ cm. Francis et al. [1998] further defined a A-D relation from the same field experiments, which holds for $D \geq 128 \times 10^{-4}$ cm, while a spherical assumption can be used for smaller particles. For the analytical integration of mass and area over PSD, we compute a single set of $a$, $b$, $\gamma$, and $\delta$ valid for all sizes of $D$ (case (3) of Table 1). In doing so, we compute $m(D)$ for $1\times 10^{-4}$ cm $\leq D \leq 200 \times 10^{-4}$ cm, using Eq. (1) with coefficients $a$ and $b$ (cases (1) and (2) of Table 1). Then linear regression is performed between $\ln(D)$ and $\ln[m(D)]$ to get coefficients $a$ and $b$ (case (3) of Table 1). Similarly, coefficients $\gamma$ and $\delta$ (case (3) of Table 1) are obtained from linear regression between $\ln(D)$ and $\ln[A(D)]$. Obtained correlation coefficients are > 0.99, and root mean square (RMS) errors for mass and area are $2.33 \times 10^{-7}$ g and $8.49 \times 10^{-6}$ cm$^2$, respectively. Hereafter, the single coefficient set of $a$, $b$, $\gamma$, and $\delta$ for all size $D$ (case (3) in Table 1) is referred to as *Brown and Francis*.

While Brown and Francis [1995] and Francis et al. [1998] provide fixed m-D and A-D relations regardless of temperature, Heymsfield et al. [2013] provide temperature-dependent m-D and A-D relations based on a wide geographical range of field experiments from Tropics through Arctic as

$$a = 0.0081 \exp(0.013\, T)\ , \tag{3}$$

$$b = 2.31 + 0.0054\, T\ , \tag{4}$$

$$\gamma = \frac{\pi}{4}(0.2833 + 0.006913T + 8.09 \times 10^{-5}\, T^2)\ , \text{ and} \tag{5}$$

$$\delta = -0.2026 + 0.009681T + 1.19 \times 10^{-4}\, T^2 + 2\ , \tag{6}$$

where $T$ is the temperature in Celsius, and $-86°\mathrm{C} \leq T \leq 0°\mathrm{C}$. We consider three different temperatures as −30°C, −45°C, and −60°C to get $a$, $b$, $\gamma$, and $\delta$ in Table 1 (cases (4)–(6)).

Yang et al. [2000] computed the mass and area of ice particles for plates, hexagonal columns, and bullets. Table 2 of Yang et al. [2000] provides coefficients of fourth order polynomials of $\ln(D)$ to compute the mass and area. Using these fourth order polynomials, we compute $m(D)$ and $A(D)$ over the size range $1\times 10^{-4}$ cm $\leq D \leq 200 \times 10^{-4}$ cm, and derive coefficients $a$, $b$, $\gamma$, and $\delta$ by linear regression (cases (7)–(9) of Table 1). For plates, hexagonal columns, and bullets, the correlation coefficients between original values and obtained values are > 0.99, and RMS errors for mass and area are $< 9.96 \times 10^{-8}$ g and $< 2.79 \times 10^{-6}$ cm$^2$, respectively.

In addition, using single particle shape properties of Yang et al. [2000], the mass and area of habit mixtures are also derived in this study, while similar work had been performed in Deng et al. [2010, 2013]. We use habit fractions defined in Baum et al.

[2005a, b]; For $D < 60 \times 10^{-4}$ cm, 100% droxtals, and for $60 \times 10^{-4}$ cm $\leq D < 1000 \times 10^{-4}$ cm, 15% of 6-branch bullets, 50% of solid hexagonal columns, and 35% of plates are assumed. The coefficients $a$, $b$, $\gamma$, and $\delta$ for mixtures are given in case (10) of Table 1, while RMS errors for mass and area are $9.88 \times 10^{-8}$ g and $8.86 \times 10^{-6}$ cm$^2$, respectively

Case (11) of Table 1 provides coefficients of power laws for spherical particles, with an assumption of solid ice density ($\rho_i$) as 0.917 g cm$^{-3}$. Therefore, $a = \rho_i \pi/6$, $b = 3$, $\gamma = \pi/4$, and $\delta = 2$.

Figure 1 shows the mass and projected area of ice particles as a function of $D$ from $a$, $b$, $\gamma$, and $\delta$ listed in Table 1. As expected a spherical particle has a larger mass and a projected area than nonspherical particles for a given $D$. Among nonspherical particles used in this study, the mass and projected area by *Brown and Francis* are closest to those for spherical particles. Bullet with 6 branches by Yang et al. [2000] has the smallest mass and projected area for a given $D$. Temperature-dependent particle shapes described by Heymsfield et al. [2013] show that the mass decreases, and projected area slightly increases with increasing temperature (−60°C to −30°C).

Figure 2 shows how the different m-D and A-D relationships, which are determined by particle shape, affect effective radius ($r_{eff}$) retrievals. As discussed in Section 2.2, radar reflectivity factor of a particle is proportional to $m(D)^2$. Therefore, total reflectivity of $N_T$ number of particles with a size $D$ is proportional to $m(D)^2 \times N_T$. In addition, the extinction coefficient of $N_T$ particles at visible wavelengths is given by $Q_{ext}\, A(D) \times N_T$, where $Q_{ext}$ is extinction efficiency at visible wavelengths. If we take the ratio of reflectivity to the extinction coefficient, $N_T$ is canceled out, and the ratio is proportional to $m(D)^2/A(D)$. Moreover, the effective radius is proportional to $m(D)/A(D)$ (Section 2.2). Therefore, Fig. 2 shows a relationship between radar reflectivity to lidar-radar ratio [$\sim m(D)^2/A(D)$] and effective radius [$\sim m(D)/A(D)$]. In this figure, plates and bullets by Yang et al. [2000] produce the smallest effective radius for a given lidar-radar ratio. In contrast, Heymsfield et al. [2013] at $T = -60$°C gives the largest cloud effective radius for $m(D)^2/A(D) < 0.03 \times 10^{-7}$ g$^2$ cm$^{-2}$, while spherical assumption gives the largest effective radius for $m(D)^2/A(D) > 0.03 \times 10^{-7}$ g$^2$ cm$^{-2}$. In Sections 3 and 4, we consider more realistic particle size distributions (PSDs) with gamma and lognormal distributions.

However, similar conclusions are found to those obtained from the single particle size assumption shown in Fig. 2.

Note that several m-D and A-D relationships considered in this study were obtained from in-situ measurements [Brown and Francis, 1995; Francis et al., 1998; Heymsfield et al., 2013]. Recent studies [Field et al., 2006; Lawson, 2011; Korolev and Field, 2015] have reported that shattered ice fragments by instruments artificially increase the number of small particles. In this study, we only use particle shape parameters ($a$, $b$, $\gamma$, and $\delta$) instead of number concentrations [$N(D)$] from the in-situ measurements. Therefore, the impacts of shattering artifacts would be relatively small, once the particle shapes of large ice particles are properly measured. Examining impacts of shattering effects on the m-D and A-D relationships remains a topic of future work.

**2.2. Size-integrated optical parameters**

In a Rayleigh-scattering regime, the equivalent radar reflectivity factor of ice particles can be computed [Brown et al., 1995; Schneider and Stephens, 1995; McFarlane and Evans, 2004; Hogan et al., 2006a, 2006b] as

$$Z_{e,Ray} = \frac{|K_i|^2}{|K_w|^2}\frac{36}{\pi^2 {\rho_i}^2}\int [m(D)]^2\, N(D)dD \tag{7}$$

where $Z_{e,Ray}$ is the equivalent radar reflectivity factor with Rayleigh scattering theory, $|K_i|^2$ is the dielectric factor of solid ice, $|K_w|^2$ is the dielectric factor of water, $N(D)$ is the number of particles with the particle size $D$ in a unit volume (cm$^{-3}$ cm$^{-1}$), $m$ is the mass in gram, and $\rho_i$ is the density of solid ice (g cm$^{-3}$). However, for ice particles > 100 μm, Mie scattering is not negligible and the effect should be considered in 94-GHz (3.2 mm) radar measurements. In this study, we use a Mie correction factor by following Benedetti et al. [2003] and Austin et al. [2009] as

$$Z_e = f_{Mie} Z_{e,Ray} = f_{Mie}\frac{|K_i|^2}{|K_w|^2}\frac{36}{\pi^2 {\rho_i}^2}\int [m(D)]^2\, N(D)dD \tag{8}$$

where $Z_e$ includes both Mie and Rayleigh scattering effects, and $f_{Mie}$ is the Mie correction factor. $f_{Mie}$ is 1 is for small ice particles (< 100 μm), and it decreases with an increasing ice particle size [Austin et al., 2009]. In addition, we define the radar reflectivity factor of ice particles ($Z$), which can be inferred from $Z_e$ using the dielectric factors [Smith, 1984; Atlas, 1995]:

$$Z = \frac{|K_w|^2}{|K_i|^2} Z_e = f_{Mie} \frac{36}{\pi^2 {\rho_i}^2} \int [m(D)]^2 N(D) dD \ . \qquad (9)$$

Combining Eqs. (1) and (9), we obtain

$$Z = \frac{36 f_{Mie}}{\pi^2 {\rho_i}^2} a^2 \int D^{2b} N(D) dD \ . \qquad (10)$$

The cloud extinction coefficient ($k_{ext}$, in the unit of $cm^{-1}$) at a visible wavelength is an integration of the extinction cross section over the PSD,

$$k_{ext} = \int A(D) N(D) Q_{ext} dD = 2\gamma \int D^{\delta} N(D) dD \ , \qquad (11)$$

where $Q_{ext}$ is the visible extinction efficiency, and approximated as 2 in this study. IWC ($g\ cm^{-3}$) is the total ice mass in a unit volume, which is an integration of $m(D)$ over PSD [e.g., Bouldala et al., 2002; McFarlane and Evans, 2004],

$$IWC = \int m(D) N(D) dD = a \int D^b N(D) dD \ . \qquad (12)$$

In this study, effective radius ($r_{eff}$, in the unit of cm) is defined as [Foot, 1988; Brown et al., 1995; Hogan et al., 2006a, 2006b; Donovan and Van Lammeren, 2001; Delanoë and Hogan, 2008]:

$$r_{eff} = \frac{IWC}{k_{ext}} \frac{3}{2\rho_i} \ . \qquad (13)$$

## 2.3. Assumptions made in this study

Most importantly, we assume that the unattenuated radar reflectivity factor ($Z$) and visible extinction ($k_{ext}$) by cloud particles are available from radar and lidar measurements, respectively. In obtaining the unattenuated reflectivity factor from the radar measurements, attenuation by gas and hydrometeors should be corrected [Marchand et al., 2008]. The gas attenuation can be estimated directly from temperature and humidity profiles based on satellite infrared/microwave sounding observations or reanalysis [e.g. Aumann et al., 2003; Tobin et al., 2006; Rienecker et al., 2011]. The attenuation by ice-phase hydrometeors is negligible since imaginary part of the refractive index of ice is in the order of $10^{-3}$ at 94 GHz (3.2 mm). Multiple scattering of the radar signal by cloud particles is generally negligible for non-precipitating clouds [Battaglia et al., 2005, 2007; Lebsock, 2011]. Therefore, we target non-precipitating clouds in this study.

If an ice particle is larger than 100 μm, the particle is not a Rayleigh scatterer anymore. In this study, we use a Mie correction factor ($f_{Mie}$) to take into account Mie scattering, following approaches of Benedetti et al. [2003] and Austin et al. [2009]. In their studies, $f_{Mie}$ is parameterized with the width parameter ($\omega$) and geometrical diameter ($D_g$) of a lognormal PSD. When $D_g$ is 100 μm, Eqs. (14)–(17) of Austin et al. [2009] give $f_{Mie} \sim 0.9$. This approach can be applied for other PSDs, such as a gamma PSD for which $f_{Mie}$ is parameterized with dispersion ($\mu$) and slope parameters ($\Lambda$). Therefore, we assume that $f_{Mie}$ is not a function of $D$. A more sophisticated formula that takes into account Mie scattering in a radar wavelength can be developed for future applications.

While direct measurements of the extinction coefficient are available from High Spectral Resolution Lidar (HSRL) or Raman lidar [Burton et al., 2012, Whiteman et al., 2004; Haarig et al., 2016], lidar ratio and multiple scattering factors are required to compute the extinction coefficient from elastic backscatter lidars such as CALIOP [Platt, 1979; Platt et al., 1998; Young and Vaughan, 2009]. The lidar ratio and multiple scattering factor can be estimated and evaluated from two-transmission method [Young and Vaughan, 2009], from comparisons with other independent observations [Garnier et al., 2015, Holz et al. 2016], or by an iteration method [Hogan et al., 2006a; Seifert et al., 2007; Kienast-Sjögren et al. 2016]. Once reasonable lidar ratio and multiple scattering factors are determined, attenuation by hydrometeors can be estimated, provided that Rayleigh scattering by gas molecules is already corrected using the atmospheric profiles. Young and Vaughan [2009] and Hogan et al. [2006a] provide detailed discussions of how the visible extinction coefficient is estimated from lidar backscatter measurements.

The density of solid ice changes up to 1% with temperature. Cloud ice particles, however, can have a much smaller density than the solid ice particle due to porosities (or bubbles). Sato and Okamoto [2006] defined the ice bulk density ($\rho_b$) as a ratio of ice mass to exterior volume of ice particle including air bubbles. If there is no bubble in the ice particle, $\rho_b$ becomes a density of solid ice around 0.917 g cm$^{-3}$, but measured $\rho_b$ is actually around 0.81 g cm$^{-3}$ [Sato and Okamoto, 2006]. Heymsfield et al. [2004] defined an effective density ($\rho_e$) as a ratio of ice mass to volume of the circumscribed sphere of a nonspherical particle. They found that $\rho_e$ can be related to the slope ($\Lambda$) of a gamma PSD. The range of $\rho_e$ shown in Heymsfield et al. [2004] is quite large; 0.15 g cm$^{-3}$ to 0.91 g cm$^{-3}$. Note that $\rho_e$ is smaller than $\rho_b$, since $\rho_e$ uses the enclosed sphere volume of nonspherical ice particle, while $\rho_b$ uses the exterior volume of a nonspherical ice particle. In this study, we assume the ice bulk density ($\rho_b$) to equal the density of solid ice (= 0.917 g cm$^{-3}$, $\rho_i$) because a change of $\rho_b$ from 0.60 to 0.92 g cm$^{-3}$ only causes <1 dB differences in the radar reflectivity [Sato and Okamoto, 2006]. However, we take into account variations of the effective density ($\rho_e$) by considering different ice particle shapes (or m-D and A-D relations).

The phase identification is important in estimating radar reflectivity ($Z$) from equivalent radar reflectivity factor ($Z_e$) (Eq. (9)). We assume that cloud particles are all in ice phase and no mixed phase is involved. In addition, the expression we derive here requires that both radar and lidar signals are available, i.e. a cloud layer needs to be optically thin so that it does not fully attenuate the lidar signal. Further studies are required to extend our expressions to lidar- or radar-only observations.

In the following sections, we examine how coefficients in m-D and A-D relations affect the retrieved effective radius in the radar and lidar observations. The retrieval algorithm is generally based on an inversion method that starts with an initial guess. The algorithm goes through iterations to minimize a cost function till the cost function becomes smaller than a threshold value. Optimal Estimation allows quantification of the retrieval errors, once uncertainties of input empirical data are known. Even though estimating the uncertainties of input data is also challenging [Mace and Benson, 2017], we assume that the inversion method converges to a solution with a reasonable accuracy. Then the analytic relationship derived here can be used for converting the effective radius derived with different particle shape assumptions to the effective radius with a common particle shape assumption for consistent radiative transfer computations.

Lastly, this study uses power laws to express distributions of mass and projected area as in Eqs. (1) and (2). Erfani and Mitchell [2016] noted that the power laws can overestimate particle mass and area for small particle sizes. They found that the second-order polynomials as functions of ln(D) are more feasible to describe mass and projected area of ice particles over the diverse range of $D$. However, because the power laws can be handled easily in analytic integrations of mass and projected area over PSD, we use the power laws throughout this study.

## 3. Analytic derivation using a gamma particle size distribution (PSD)

In this section, we consider a gamma size distribution in deriving radar reflectivity factor ($Z$), ice water content (IWC), visible extinction coefficient ($k_{ext}$), and effective radius ($r_{eff}$). Then the sensitivity of $r_{eff}$ to coefficients of m-D and A-D relationships is analytically examined. We also show similar derivations with a lognormal size distribution in Section 4.

### 3.1. Sensitivity of $r_{eff}$ and IWC to coefficients of m-D and A-D relationships

The gamma particle size distribution (PSD) [e.g., Kosarev and Mazin, 1991; Mitchell, 1991] is defined as

$$N(D) = N_0 D^{\mu} \exp(-\Lambda D) \,, \tag{14}$$

where $\Lambda$ is the slope ($cm^{-1}$), $\mu$ is the dispersion (unitless), and $N_0$ ($cm^{-\mu-4}$) is the intercept.

In this equation, $N(D)$ decreases more rapidly toward large $D$ with increasing $\Lambda$, and the inflection point of $N(D)$ moves toward zero with decreasing $\mu$. This means that the particle effective radius decreases with increasing $\Lambda$ or decreasing $\mu$. The $j$th Moment Generating Function (MGF) of gamma distribution is

$$M_j = \int N(D) D^j dD = N_0 \frac{\Gamma(j+\mu+1)}{\Lambda^{j+\mu+1}} \,. \tag{15}$$

The total number ($N_T$) of the gamma distribution in the unit of $cm^{-3}$ is obtained from the zeroth moment of MGF:

$$N_T = N_0 \frac{\Gamma(\mu+1)}{\Lambda^{\mu+1}} \,. \tag{16}$$

Combining Eqs. (10) and (15), the radar reflectivity factor in the unit of $cm^6\ cm^{-3}$ (= $10^{12}$ $mm^6\ m^{-3}$) is

$$Z = \frac{36 f_{Mie}}{\pi^2 \rho_i^2} a^2 N_0 \frac{\Gamma(2b+\mu+1)}{\Lambda^{2b+\mu+1}} \,. \tag{17}$$

Similarly, $k_{ext}$ ($cm^{-1}$), $IWC$ ($g\ cm^{-3}$), and $r_{eff}$ (cm) are expressed as

$$k_{ext} = 2 N_0 \gamma \frac{\Gamma(\delta+\mu+1)}{\Lambda^{\delta+\mu+1}} \,, \tag{18}$$

$$IWC = a N_0 \frac{\Gamma(b+\mu+1)}{\Lambda^{b+\mu+1}} \text{ , and} \tag{19}$$

$$r_{eff} = 3 a N_0 \frac{\Gamma(b+\mu+1)}{\Lambda^{b+\mu+1}} \frac{1}{4 \rho_i N_0 \gamma} \frac{\Lambda^{\delta+\mu+1}}{\Gamma(\delta+\mu+1)} = \frac{3a}{4 \rho_{si} \gamma} \frac{\Gamma(b+\mu+1)}{\Gamma(\delta+\mu+1)} \Lambda^{\delta-b} . \tag{20}$$

Once we take the ratio of $Z$ to $k_{ext}$ (radar reflectivity-to-lidar-extinction ratio), $N_0$ cancels out and results in

$$\frac{Z}{k_{ext}} = \frac{18 f_{Mie}}{\pi^2 \rho_i^2} \frac{a^2}{\gamma} \frac{\Gamma(2b+\mu+1)}{\Gamma(\delta+\mu+1)} \Lambda^{\delta-2b} \ . \quad (21)$$

where $Z/k_{ext}$ is in the unit of cm$^4$. Figure 3 shows a typical range of $Z/k_{ext}$ using CloudSat and CALIPSO measurements. CloudSat provides equivalent radar reflectivity factor in dB ($Z_{dB}$) (Fig. 3a), where $Z_{dB} = 10 \log Z_e$. Then Eq. (9) can be used to obtain radar reflectivity ($Z$) from equivalent radar reflectivity factor ($Z_e$). Combining CloudSat $Z$ with CALIPSO cloud extinction coefficient ($k_{ext}$) results in $Z/k_{ext}$ in Fig. 3c for ice clouds. The ice clouds are selected when $k_{ext} > 0.01$ km$^{-1}$ and air temperature < 253 K. $Z/k_{ext}$ generally increases with $Z$ (Fig. 3d), and $Z/k_{ext}$ is between $10^{-10}$ and $10^{-6}$ cm$^4$ (Fig. 3e).

In Eqs. (20) and (21), $r_{eff}$ and $Z/k_{ext}$ are expressed with $a$, $b$, $\gamma$, $\delta$, $\mu$, and $\Lambda$. Note that impacts of $\mu$ and $\Lambda$ largely offset in $N(D)$ for a given $D$, since $N(D)$ increases with increasing $\mu$ and with decreasing $\Lambda$. Either $\mu$ or $\Lambda$ in above equations can be eliminated using Eq. (21). To eliminate $\Lambda$, we solve Eq. (21) for $\Lambda$

$$\Lambda = \left\{\frac{Z}{k_{ext}} \frac{\pi^2 \rho_i^2}{18 f_{Mie}} \frac{\gamma}{a^2} \frac{\Gamma(\delta+\mu+1)}{\Gamma(2b+\mu+1)}\right\}^{\frac{1}{\delta-2b}} , \quad (22)$$

and substitute Eq. (22) into Eq. (20) to obtain

$$r_{eff} = \frac{3a}{4\rho_i \gamma} \frac{\Gamma(b+\mu+1)}{\Gamma(\delta+\mu+1)} \left\{\frac{Z}{k_{ext}} \frac{\pi^2 \rho_i^2}{18 f_{Mie}} \frac{\gamma}{a^2} \frac{\Gamma(\delta+\mu+1)}{\Gamma(2b+\mu+1)}\right\}^{\frac{b-\delta}{2b-\delta}} . \quad (23)$$

Resulting Eq. (23) is a function of $a$, $b$, $\gamma$, $\delta$, and $\mu$. Using asymptotic theory, we get

$$\left(\frac{\Gamma(x+p)}{\Gamma(x+q)}\right) \sim \left(x + \frac{p+q-1}{2} + o(x^{-1})\right)^{p-q} \quad as\ x \to \infty \ , \quad (24)$$

where $x = \mu + \delta + 1$, $p = b - \delta$, and $q = 0$ (see Appendix A for more detailed expressions). When using the first two terms in the right side of Eq. (24) and ignoring higher terms, errors are <15%, <4%, and <2% for $\mu \geq -2$, $\mu \geq 0$, and $\mu \geq 2$, respectively (Appendix A, Fig. A1). Using Eq. (24), we can approximate Eq. (23) as

$$r_{eff} = \frac{3a}{4\rho_i \gamma} \left\{\mu + \frac{b+\delta+1}{2}\right\}^{b-\delta} \left\{\frac{Z}{k_{ext}} \frac{\pi^2 \rho_i^2}{18 f_{Mie}} \frac{\gamma}{a^2}\right\}^{\frac{b-\delta}{2b-\delta}} \left\{\mu + \frac{2b+\delta+1}{2}\right\}^{-b+\delta}$$

$$= \frac{3}{4\rho_i} a^{\frac{\delta}{2b-\delta}} \ \gamma^{-\frac{b}{2b-\delta}} \left\{\frac{Z}{k_{ext}} \frac{\pi^2 \rho_i^2}{18 f_{Mie}}\right\}^{\frac{b-\delta}{2b-\delta}} \left\{\frac{2\mu+b+\delta+1}{2\mu+2b+\delta+1}\right\}^{b-\delta} . \quad (25)$$

Note that this approximated Eq. (25) is only used for analytic expressions of the first derivatives in Eqs. (27)−(30), and (32). Full equation Eq. (23) is used for all other derivations. We take the natural logarithm of Eq. (25),

$$\ln r_{eff} = \ln\frac{3}{4\rho_i} + \frac{\delta}{2b-\delta}\ln a - \frac{b}{2b-\delta}\ln\gamma + \left(\frac{b-\delta}{2b-\delta}\right)\ln\left(\frac{Z}{k_{ext}}\frac{\pi^2{\rho_i}^2}{18f_{Mie}}\right) + (b - \delta)\ln\left(\frac{2\mu+b+\delta+1}{2\mu+2b+\delta+1}\right), \quad (26)$$

where $Z$ and $k_{ext}$ are known values since they are assumed to be available from the radar and lidar measurements (Section 2.3). We assume that $\mu$ is not a function of $a$, $b$, $\gamma$, and $\delta$ (i.e. the size distribution does not depend on particle shape) and take derivatives of $r_{eff}$ with respect to $a$, $b$, $\gamma$, and $\delta$. These derivatives can be interpreted as a sensitivity of $r_{eff}$ to assumption of particle shape factor, in terms of $a$, $b$, $\gamma$, and $\delta$. The first derivatives of Eq. (26) with respect to $a$, $b$, $\gamma$, and $\delta$ are

$$\frac{\partial(\ln r_{eff})}{\partial a} = \frac{\delta}{2b-\delta}\frac{1}{a}, \quad (27)$$

$$\frac{\partial(\ln r_{eff})}{\partial b} = \frac{\delta}{(2b-\delta)^2}\ln\left(\frac{Z}{k_{ext}}\frac{\pi^2{\rho_i}^2}{18f_{Mie}}\frac{\gamma}{a^2}\right) + \ln\left(\frac{2\mu+b+\delta+1}{2\mu+2b+\delta+1}\right) - \frac{(b-\delta)(2\mu+\delta+1)}{(2\mu+b+\delta+1)(2\mu+2b+\delta+1)}, \quad (28)$$

$$\frac{\partial(\ln r_{eff})}{\partial \gamma} = -\frac{1}{\gamma}\frac{b}{2b-\delta}, \text{ and} \quad (29)$$

$$\frac{\partial(\ln r_{eff})}{\partial \delta} = -\frac{b}{(2b-\delta)^2}\ln\left(\frac{Z}{k_{ext}}\frac{\pi^2{\rho_i}^2}{18f_{Mie}}\frac{\gamma}{a^2}\right) - \ln\left(\frac{2\mu+b+\delta+1}{2\mu+2b+\delta+1}\right) + \frac{b(b-\delta)}{(2\mu+b+\delta+1)(2\mu+2b+\delta+1)}. \quad (30)$$

Equation (27) > 0, Eq. (28) < 0, Eq. (29) < 0, and Eq. (30) > 0, because $a > 0$, $b > \delta > 0$, $\gamma > 0$, and $0 < \frac{Z}{k_{ext}}\frac{\pi^2{\rho_i}^2}{18f_{Mie}}\frac{\gamma}{a^2} < 1$. Therefore, $r_{eff}$ increases with increasing $a$, decreasing $b$, decreasing $\gamma$, or increasing $\delta$.

Figure 4 shows the sensitivity of $r_{eff}$ for changing $a$, $b$, $\gamma$, and $\delta$ by ±10% using Eq. (23). We set reference values of $a$, $b$, $\gamma$, and $\delta$ using *Brown and Francis* (case (3) of Table 1). Then two of four parameters $a$, $b$, $\gamma$, and $\delta$ are perturbed by 10% from the reference values in each panel of Fig. 4. We consider two values of $Z/k_{ext}$ in Eq. (23), $10^{-10}$ and $10^{-6}$ $cm^4$, which are, respectively, the lower and upper limit of a typical range (Fig. 3e). Also, $\mu$ is fixed as −1 in Fig. 4. The sensitivity of $r_{eff}$ to $\mu$ is separately examined in Section 3.2. In addition, $f_{Mie}$ is fixed as 1 in Fig. 4. For $D_g$ = 100 μm in the lognormal PSD, $f_{Mie}$ is around 0.9 (Section 2.3). If we use $f_{Mie}$ of 0.9 instead of 1, $r_{eff}$ shows almost the same sensitivity to $a$, $b$, $\gamma$, and $\delta$ (not shown).

Figure 4 shows that retrieved $r_{eff}$ increases with increasing $a$, with decreasing $b$, with decreasing $\gamma$, or with increasing $\delta$, which are consistent with signs of Eqs. (27)−(30). Both $Z/k_{ext} = 10^{-10}$ and $10^{-6}$ cm$^4$ show almost the same sensitivity of $r_{eff}$ to $a$, $b$, $\gamma$, and $\delta$. The 10% changes of $a$, $b$, $\gamma$, and $\delta$ can change $r_{eff}$ by more than 100% (each panel of Fig. 4). In particular, $r_{eff}$ is more sensitive to $b$ and $\delta$, in comparison to $a$ and $\gamma$, simply because $b$ and $\delta$ are exponents for mass and projected area distributions, while $a$ and $\gamma$ are scaling factors.

Figure 5 represents computed $r_{eff}$ using Eq. (23) for different sets of $a$, $b$, $\gamma$, and $\delta$ listed in Table 1. Similar to Fig. 4, $\mu$ is fixed as −1, but $Z/k_{\mathrm{ext}}$ changes from $10^{-10}$ to $10^{-6}$ cm$^4$. In addition, $f_{Mie}$ is assumed to be 1 in Fig. 5. When $f_{Mie}$ is assumed to be 0.9 (Section 2.3), the retrieved $r_{eff}$ is 1.5–3% larger than $r_{eff}$ with $f_{Mie} = 1$ (not shown). This is simply because $r_{eff}$ is proportional to $f_{Mie}^{-(b-\delta)/(2b-\delta)}$ in Eq. (23), while $-(b-\delta)/(2b-\delta)$ changes between –0.15 and –0.25 depending on m-D and A-D relationships.

The vertical spread of curves in Fig. 5 is basically the uncertainty in the retrieved $r_{eff}$ due to ice particle shape ($a$, $b$, $\gamma$, and $\delta$) assumptions. When $Z/k_{ext} < 10^{-7}$ cm$^4$, the particle shape of Heymsfield et al. [2013] at $T = -60$°C gives the largest $r_{eff}$, while plates and bullets of Yang et al. [2000] give the smallest $r_{eff}$. For $Z/k_{ext} < 10^{-8}$ cm$^4$, $r_{eff}$ derived with Heymsfield et al. [2013] at the temperature of −60°C is almost twice of $r_{eff}$ derived with plates or bullets of Yang et al. [2000]. These results are consistent with Fig. 2, in which size distribution is not considered (i.e. mono-disperse). This suggests that relative changes of $r_{eff}$ due to different $a$, $b$, $\gamma$, and $\delta$ might not be limited to a specific PSD assumption.

A similar type of comparisons to those in this section was performed by Donovan and Van Lammeren [2001]. Figure 10 of Donovan and Van Lammeren [2001] shows that an assumption of spherical particles leads to the largest $r_{eff}$, while compact polycrystal leads to the smallest $r_{eff}$ for the given $r_{eff}'$, where $r_{eff}'$ is defined from the radar-to-lidar ratio.

The sensitivity of $IWC$ to ice particle shape can be computed by multiplying Eqs. (27) –(30) by $\partial(\ln IWC)/\partial(\ln r_{eff})$. Note that $IWC$, $k_{ext}$, and $r_{eff}$ are related by Eq. (13), and $k_{ext}$ is fixed because it is known from the lidar measurements. Therefore, $\partial(\ln k_{ext}) = 0$, and $\partial(\ln IWC) = \partial(\ln r_{eff})$ or $\partial(\ln IWC)/\partial(\ln r_{eff}) = 1$. This suggests that $IWC$ has the same sensitivity to $a$, $b$, $\gamma$, and $\delta$ as $r_{eff}$.

### 3.2. Sensitivity of $r_{eff}$ to assumption of $\mu$

When the sensitivity of $r_{eff}$ to m-D and A-D relationships (in terms of $a$, $b$, $\gamma$, and $\delta$) is analyzed in Section 3.1, $\mu$ is fixed as −1. Data from field campaigns suggest that $\mu$ varies between −2 to 10 [Heymsfield et al., 2002, 2013; Patade et al., 2015; Hou et al., 2014]. In this section, we examine how $\mu$ in the gamma PSD influences the solution of $r_{eff}$.

Instead of fixing $\mu$ as −1, we can simultaneously retrieve $\mu$ along with other parameters. The problem with this approach is that we have three unknowns, $N_0$, $\mu$, and $\Lambda$, to fully describe the gamma PSD, but we only have two measured values of radar reflectivity factor ($Z$) and visible extinction ($k_{ext}$). This means that $N_0$, $\mu$, and $\Lambda$ are not uniquely determined. As a result, the radar and lidar algorithm requires additional information to constrain the solution of $N_0$, $\mu$, and $\Lambda$. Since our derivation of $r_{eff}$ in Eq. (23) includes $\mu$, we can use a relationship between $\mu$ and temperature based on in-situ measurements [Heymsfield et al., 2013]:

$$\mu = -0.84 - 0.0915\,T - 2.936 \times 10^{-3}\,T^2 - 3.653 \times 10^{-5}\,T^3 - 2.157 \times 10^{-8}\,T^4\,, \quad (31)$$

where $T$ is the temperature in Celsius between −86°C and 0°C. Note that in Fig. 9 of Heymsfield et al. [2013], actual $\mu$ deviates up to ±2 from the temperature-based value in Eq. (31). This suggests that constraining $\mu$ with Eq. (31) brings uncertainties of $\mu$ by ±2.

The sensitivity of $r_{eff}$ to $\mu$ can be obtained from the first derivative of $r_{eff}$ with respect to $\mu$:

$$\frac{\partial \ln r_{eff}}{\partial \mu} = \frac{(b-\delta)}{(2\mu+b+\delta+1)}\frac{2b}{(2\mu+2b+\delta+1)}\;. \quad (32)$$

Eq. (32) is positive, and only a function of $\mu$, $b$ and $\delta$, but not $a$ and $\gamma$. The sensitivity increases with increasing $b$, decreasing $\delta$, or decreasing $\mu$. If $b = \delta$ or $b = 0$, Eq. (32) is zero, and the solution of $r_{eff}$ is not affected by the choice of $\mu$. These conditions are, however, unrealistic (Appendix B).

Figure 6 shows how much $r_{eff}$ changes when $\mu$ is increased by 2, considering the actual $\mu$ can deviate from temperature-based $\mu$ (Eq. (31)) by up to ±2. In addition, $f_{Mie}$ is assumed to be 1 because $f_{Mie}$ does not change $r_{eff}(\mu+2)/r_{eff}(\mu)$. In Fig. 6, the sensitivity of $r_{eff}$ to $\mu$ [$=\partial(ln\ r_{eff})/\partial\mu$] is larger for a smaller $\mu$, which is consistent with Eq. (32). Among m-D and A-D relationships in Fig. 6, the ice mixture by Yang et al. [2000] shows the largest sensitivity, while the particle shape of Heymsfield et al. [2013] at −60°C shows the smallest sensitivity. This is because the mixture by Yang et al. [2000] has the largest coefficient *b*, while the particle shape of Heymsfield et al. [2013] at −60°C has the smallest *b*, which essentially determines the magnitude of Eq. (32).

In Fig. 6, a large uncertainty of $r_{eff}$ occurs for $\mu_0 < 0$, resulting ratios of $r_{eff}$ ($\mu = \mu_0+2$) to $r_{eff}$ ($\mu = \mu_0$) > 1.2. This means that >20% errors in $r_{eff}$ are expected when increasing $\mu$ by 2. However, when $\mu_0$ is positive in Fig. 6, most of the shapes show the ratio less than 1.1 (<10% errors in $r_{eff}$). The negative disperse ($\mu$) means a sub-exponential particle size distribution, which is often associated with small ice particles or smaller $\Lambda$ [Patade et al., 2015]. In other words, when ice clouds are predominantly composed of larger ice particles, $\mu > 0$ and $r_{eff}$ is relatively insensitive to the assumption of $\mu$. In addition, Fig. 9b of Patade et al. [2015] shows a strong relationship between $\mu$ and $\Lambda$ for subdivided temperature ranges. This suggests that the uncertainty of $r_{eff}$ due to the assumption of $\mu$ can be significantly reduced if the relationship between $\mu$ and $\Lambda$ is used in the retrievals.

## 4. Analytic derivation using a lognormal PSD

In this section, we derive size-integrated optical parameters using a lognormal PSD, and the results are compared with those from the gamma PSD (Section 3). We consider the lognormal PSD as follows:

$$N(D) = N_T \frac{1}{\sqrt{2\pi}\omega D} \exp\left[-\frac{(\ln D - \ln D_g)^2}{2\omega^2}\right]. \tag{33}$$

where $N_T$ is a total number of particles in a unit volume (cm$^{-3}$), $D_g$ is a geometrical diameter (cm), and $\omega$ is a width parameter (unitless). The *j*th Moment Generating Function (MGF) of the lognormal distribution is given by

$$M_j = \int N(D) D^j dD = N_T {D_g}^j \exp\left(\frac{1}{2} j^2 \omega^2\right). \tag{34}$$

If we apply Eq. (34) to Eqs. (10)−(13), we get

$$Z = \frac{36 f_{Mie}}{\pi^2 {\rho_i}^2} a^2 N_T {D_g}^{2b} \exp(2b^2\omega^2), \tag{35}$$

$$k_{ext} = 2\gamma N_T {D_g}^{\delta} \exp\left(\frac{1}{2}\delta^2\omega^2\right), \tag{36}$$

$$IWC = a N_T {D_g}^{b} \exp\left(\frac{1}{2} b^2 \omega^2\right), \text{ and} \tag{37}$$

$$r_{eff} = \frac{3}{4\rho_i}\frac{a}{\gamma} D_g{}^{b-\delta} \exp\left(\frac{1}{2}(b^2-\delta^2)\omega^2\right). \quad (38)$$

The ratio $Z/k_{ext}$ can be expressed as a function of $a$, $b$, $\gamma$, $\delta$, $D_g$, and $\omega$:

$$\frac{Z}{k_{ext}} = \frac{18 f_{Mie}}{\pi^2 \rho_i{}^2}\frac{a^2}{\gamma} D_g{}^{2b-\delta} \exp\left(\frac{4b^2-\delta^2}{2}\omega^2\right). \quad (39)$$

Note that for a given $D$, impacts of $D_g$ and $\omega$ on $N(D)$ largely offset since $N(D)$ increases with increasing $D_g$ and with decreasing $\omega$. We can eliminate one of $D_g$ and $\omega$ using Eq. (39). Rearranging Eq. (39), we get

$$D_g = \left\{\frac{Z}{k_{ext}}\frac{\pi^2\rho_i{}^2\gamma}{18 f_{Mie} a^2}\right\}^{\frac{1}{2b-\delta}} \exp\left(-\frac{2b+\delta}{2}\omega^2\right). \quad (40)$$

Combining Eqs. (38) and (40) results in

$$r_{eff} = \frac{3}{4\rho_i}\frac{a}{\gamma}\left\{\frac{Z}{k_{ext}}\frac{\pi^2\rho_i{}^2\gamma}{18 f_{Mie} a^2}\right\}^{\frac{b-\delta}{2b-\delta}} \exp\left(-\frac{b}{2}(b-\delta)\omega^2\right). \quad (41)$$

Equation (41) becomes a function of $a$, $b$, $\gamma$, $\delta$, and $\omega$, while $D_g$ is eliminated in the equation. By taking the natural logarithm of Eq. (41),

$$\ln r_{eff} = \ln\left(\frac{3}{4\rho_i}\right) + \frac{\delta}{2b-\delta}\ln a - \frac{b}{2b-\delta}\ln\gamma + \frac{b-\delta}{2b-\delta}\ln\left\{\frac{Z}{k_{ext}}\frac{\pi^2\rho_i{}^2}{18 f_{Mie}}\right\} - \frac{1}{2}(b^2-b\delta)\omega^2. \quad (42)$$

As in Section 3, we get the first derivatives of $r_{eff}$ with respect to $a$, $b$, $\gamma$, and $\delta$:

$$\frac{\partial(\ln r_{eff})}{\partial a} = \frac{\delta}{2b-\delta}\frac{1}{a} > 0, \quad (43)$$

$$\frac{\partial(\ln r_{eff})}{\partial b} = \frac{\delta}{(2b-\delta)^2}\ln\left\{\frac{Z}{k_{ext}}\frac{\pi^2\rho_i{}^2}{18 f_{Mie}}\frac{\gamma}{a^2}\right\} - \frac{\omega^2}{2}(2b-\delta) < 0, \quad (44)$$

$$\frac{\partial(\ln r_{eff})}{\partial \gamma} = -\frac{b}{2b-\delta}\frac{1}{\gamma} < 0, \text{ and} \quad (45)$$

$$\frac{\partial(\ln r_{eff})}{\partial \delta} = -\frac{b}{(2b-\delta)^2}\ln\left\{\frac{Z}{k_{ext}}\frac{\pi^2\rho_i{}^2}{18 f_{Mie}}\frac{\gamma}{a^2}\right\} + \frac{\omega^2}{2} > 0. \quad (46)$$

Equations (43)–(46) show consistent signs to those found in Eqs. (27)–(30). In addition, Eqs. (43) and (45) are equal to Eqs. (27) and (29), respectively. This means that sensitivity of $r_{eff}$ to $a$ and $\gamma$ are the same when either gamma or lognormal PSD is used. In contrast, the sensitivity of $r_{eff}$ to $b$ and $\delta$ depends on $\mu$ in the gamma PSD and $\omega$ in the lognormal PSD.

As in the gamma PSD, the lognormal PSD has three unknown parameters $N_T$, $D_g$, and $\omega$, while we only have two measured parameters as $k_{ext}$ and $Z$. Therefore, a unique solution of $N_T$, $D_g$, and $\omega$ does not exist, and the retrieval algorithm requires additional information about $N_T$, $D_g$, or $\omega$. Since our expression of $r_{eff}$ in Eq. (41) is a function of $\omega$, we can use in-situ measurements of $\omega$ to constrain the solution [e.g., Tian et al., 2010, Austin et al., 2009]. For example, Austin et al. [2009] set up *a priori* value of $\omega$ depending on air temperature in CloudSat 2B-CWC algorithm:

$$\omega = 0.694582 + 0.00650884T \;, \quad (47)$$

where $T$ is the temperature in Celsius. Figure 7 shows that *a priori* value of $\omega$ and retrieved $\omega$ by the 2B-CWC algorithm. For each temperature level, retrieved $\omega$ deviates from *a priori* value (red line in Fig. 7) by about 0.1. Therefore, when we use the temperature-based $\omega$ in Eq. (47), the uncertainty of $\omega$ is about 0.1, and it also causes the uncertainty in $r_{eff}$. The sensitivity of $r_{eff}$ to the assumption of $\omega$ is quantified by

$$\frac{\partial(\ln r_{eff})}{\partial\omega} = -b(b-\delta)\omega \;. \quad (48)$$

Equation (48) is negative, and the magnitude increases with increasing $\omega$, increasing $b$, or decreasing $\delta$. If $b = \delta$ or $b = 0$, Eq. (48) becomes zero, and the solution of $r_{eff}$ is not affected by choice of $\omega$, but these conditions are unrealistic (Appendix B).

Figure 8 shows changes of $r_{eff}$ when $\omega$ is increased by 0.1. As in Fig. 6, $f_{Mie}$ is fixed as 1 because $f_{Mie}$ does not change $r_{eff}(\omega+0.1)/r_{eff}(\omega)$. When $\omega$ is larger, the sensitivity of $r_{eff}$ to $\omega$ is larger, which is consistent with Eq. (48). In addition, among m-D and A-D relationships used in Fig. 8, the mixture of Yang et al. [2000] shows the largest sensitivity (the largest deviation of ratio from 1), and the particle shape of Heymsfield et al. [2013] at −60°C shows the smallest sensitivity. This is consistent with those found in Section 3.2 with the gamma PSD. Generally, uncertainties of $r_{eff}$ related to the assumption of $\omega$ are smaller than 20% for all particle shapes.

# 5. Conversion of $r_{eff}$

In this section, we use analytical relationships derived in Sections 3 and 4 to demonstrate the conversion of $r_{eff}$ derived with different particle shapes (Section 5.1) or PSD (Section 5.2) assumptions. In Section 5.3, we discuss a more general case that both particle shape and PSD are different between two radar-lidar algorithms.

## 5.1. Conversions of $r_{eff}$ when different particle shapes are used in the gamma PSD

If two retrieval algorithms use the same gamma PSD, but assume different particle shapes ($a$, $b$, $\gamma$, and $\delta$), retrieved effective radii would differ as shown in Fig. 5. Let us assume that $r_{eff,1}$ is retrieved from a coefficient set of $a_1$, $b_1$, $\gamma_1$, and $\delta_1$, and $r_{eff,2}$ is retrieved from a coefficient set of $a_2$, $b_2$, $\gamma_2$, and $\delta_2$. We also assume that both algorithms use the same value $\mu$. If we want to convert $r_{eff,1}$ into $r_{eff,2}$, we can use analytic expressions discussed in Section 3. First, we can express $Z/k_{ext}$ with $r_{eff,1}$, $a_1$, $b_1$, $\gamma_1$, and $\delta_1$ using Eq. (23) as follows:

$$\frac{Z}{k_{ext}} = \left\{ r_{eff,1} \frac{4\rho_i\gamma_1}{3a_1} \frac{\Gamma(\delta_1+\mu+1)}{\Gamma(b_1+\mu+1)} \right\}^{\frac{2b_1-\delta_1}{b_1-\delta_1}} \frac{18 f_{Mie,1}}{\pi^2\rho_i^2} \frac{a_1{}^2}{\gamma_1} \frac{\Gamma(2b_1+\mu+1)}{\Gamma(\delta_1+\mu+1)} . \tag{49}$$

Combining Eqs. (23) and (49), $r_{eff,2}$ can be further expressed with $r_{eff,1}$, $a_1$, $b_1$, $\gamma_1$, and $\delta_1$, as follows:

$$\begin{aligned} r_{eff,2} &= \frac{3a_2}{4\rho_i\gamma_2} \frac{\Gamma(b_2+\mu+1)}{\Gamma(\delta_2+\mu+1)} \left\{ \frac{\pi^2\rho_i{}^2}{18 f_{Mie,2}} \frac{\gamma_2}{a_2{}^2} \frac{\Gamma(\delta_2+\mu+1)}{\Gamma(2b_2+\mu+1)} \right\}^{\frac{b_2-\delta_2}{2b_2-\delta_2}} \left\{ \frac{Z}{k_{ext}} \right\}^{\frac{b_2-\delta_2}{2b_2-\delta_2}} \\ &= r_{eff,1}{}^{\frac{2b_1-\delta_1}{b_1-\delta_1}\frac{b_2-\delta_2}{2b_2-\delta_2}} \frac{3a_2}{4\rho_i\gamma_2} \frac{\Gamma(b_2+\mu+1)}{\Gamma(\delta_2+\mu+1)} \left\{ \frac{f_{Mie,1}}{f_{Mie,2}} \frac{a_1{}^2}{\gamma_1} \frac{\gamma_2}{a_2{}^2} \right\}^{\frac{b_2-\delta_2}{2b_2-\delta_2}} \\ &\times \left\{ \frac{\Gamma(\delta_2+\mu+1)}{\Gamma(2b_2+\mu+1)} \frac{\Gamma(2b_1+\mu+1)}{\Gamma(\delta_1+\mu+1)} \right\}^{\frac{b_2-\delta_2}{2b_2-\delta_2}} \left\{ \frac{4\rho_i\gamma_1}{3a_1} \frac{\Gamma(\delta_1+\mu+1)}{\Gamma(b_1+\mu+1)} \right\}^{\frac{2b_1-\delta_1}{b_1-\delta_1}\frac{b_2-\delta_2}{2b_2-\delta_2}} . \end{aligned} \tag{50}$$

Eq. (50) gives a conversion formula from $r_{eff,1}$ to $r_{eff,2}$, or vice versa. Note that Eq. (50) becomes $r_{eff,2} = r_{eff,1}$, if two algorithms use the same set of $a$, $b$, $\gamma$, and $\delta$ (i.e. $a_1= a_2$, $b_1= b_2$, $\gamma_1= \gamma_2$, $\delta_1= \delta_2$) and Mie correction factor ($f_{Mie,1} = f_{Mie,2}$).

Figure 9 shows relationships between $r_{eff,1}$ and $r_{eff,2}$, when $r_{eff,1}$ is retrieved from the m-D and A-D relations of *Brown and Francis* (case (3) of Table 1), while $r_{eff,2}$ is retrieved from other m-D and A-D relationships shown in Table 1 (cases (4)–(11)). We also assume in Fig. 9 that the same Mie correction factor is used in two algorithms ($f_{Mie,1} = f_{Mie,2}$). In Fig. 9, we use two values of $\mu$ as 4.16 and –0.45, corresponding temperature −75°C and −5°C based on Eq. (31). However, if other values of $\mu$ are used in the retrieval algorithms, the corresponding values should be used in Eq. (50) for the effective radius conversion.

Figure 9 shows that the impact of $\mu$ on the relationship between $r_{eff,1}$ and $r_{eff,2}$ is almost negligible, as long as the same $\mu$ is applied to $r_{eff,1}$ and $r_{eff,2}$, while $r_{eff,1}$ significantly differs from $r_{eff,2}$. For the given $r_{eff,1}$, the spherical assumption or the ice particle shape by

Heymsfield et al. [2013] at $T = -60°C$ gives the largest $r_{eff,2}$, while plates or bullets from Yang et al. [2000] give the smallest $r_{eff,2}$. These results are consistent with those shown in Figs. 2 and 5.

Deng et al. [2013] showed that $r_{eff}$ from DARDAR products [Delanoë and Hogan, 2008, 2010] is greater than $r_{eff}$ from CloudSat 2C-ICE products [Deng et al., 2010, 2013, 2015]. The CloudSat 2C-ICE algorithm uses particle shape from the habit mixtures from Yang et al. [2000], while the DARDAR algorithm uses the particle shape from *Brown and Francis* [Brown and Francis, 1995, Francis et al., 1998]. Figure 9 shows that $r_{eff,2}$ derived with the habit mixtures from Yang et al. [2000] is smaller than $r_{eff,1}$ derived with the particle shape from *Brown and Francis*, for $r_{eff,1} < 120$ μm. Considering the effective radius is typically smaller than 100 μm, e.g., Fig. 10 of Deng et al. [2013], Fig. 9 is consistent with the result of Deng et al. [2013].

### 5.2. Conversions of $r_{eff}$ when different PSDs are used but with the same particle shape

In this section, we assume that two algorithms use different PSDs (gamma versus lognormal) but use the same coefficients of $a$, $b$, $\gamma$, and $\delta$. If $r_{eff,Gam}$ is retrieved with a gamma PSD, while $r_{eff,LN}$ is retrieved with a lognormal PSD, the conversion from $r_{eff,Gam}$ to $r_{eff,LN}$ can also be made using equations derived in Sections 3 and 4. Similar to the relationship derived in Section 5.1, $Z/k_{ext}$ can be expressed with $r_{eff,Gam}$, $a$, $b$, $\gamma$, and $\delta$ as in Eq. (49). This can be used to express $Z/k_{ext}$ in Eq. (41) as

$$r_{eff,LN} = \frac{3}{4\rho_i}\frac{a}{\gamma}\left\{\frac{\pi^2\rho_i{}^2\gamma}{18f_{Mie,LN}a^2}\right\}^{\frac{b-\delta}{2b-\delta}}\exp\left[-\frac{b}{2}(b-\delta)\omega^2\right]\left\{\frac{Z}{k_{ext}}\right\}^{\frac{b-\delta}{2b-\delta}}$$

$$= \frac{3}{4\rho_i}\frac{a}{\gamma}\left\{\frac{\pi^2\rho_i{}^2\gamma}{18f_{Mie,LN}a^2}\right\}^{\frac{b-\delta}{2b-\delta}}\exp\left[-\frac{b}{2}(b-\delta)\omega^2\right]$$

$$\times\left\{r_{eff,Gam}\frac{4\rho_i\gamma}{3a}\frac{\Gamma(\delta+\mu+1)}{\Gamma(b+\mu+1)}\right\}\left\{\frac{18f_{Mie,Gam}}{\pi^2\rho_i{}^2}\frac{a^2}{\gamma}\frac{\Gamma(2b+\mu+1)}{\Gamma(\delta+\mu+1)}\right\}^{\frac{b-\delta}{2b-\delta}}$$

$$= r_{eff,Gam}\exp\left[-\frac{b}{2}(b-\delta)\omega^2\right]\frac{\Gamma(\delta+\mu+1)}{\Gamma(b+\mu+1)}\left\{\frac{f_{Mie,Gam}}{f_{Mie,LN}}\frac{\Gamma(2b+\mu+1)}{\Gamma(\delta+\mu+1)}\right\}^{\frac{b-\delta}{2b-\delta}}. \quad (51)$$

Therefore, $r_{eff,LN}$ is directly proportional to $r_{eff,Gam}$, and the ratio is determined by both $\mu$ and $\omega$. Figure 10 shows the ratio of $r_{eff,Gam}$ to $r_{eff,LN}$ for various combinations of $\mu$ and $\omega$, while $a$, $b$, $\gamma$, and $\delta$ are from *Brown and Francis* (case (3) of Table 1). It is also assumed in Fig. 10 that the same Mie correction factor is used between two algorithms ($f_{Mie,LN} = f_{Mie,Gam}$). The ratio of $r_{eff,Gam}$ to $r_{eff,LN}$ is less than 1 for a smaller $\omega$ and $\mu$, indicating $r_{eff,LN}$ is larger than $r_{eff,Gam}$. In contrast, the ratio is larger than 1 for a larger $\omega$ and $\mu$, i.e. $r_{eff,Gam}$ is larger than $r_{eff,LN}$. In Eq. (51), $r_{eff,Gam}$ equals to $r_{eff,LN}$ when

$$\omega = \sqrt{\frac{2}{b(b-\delta)}\ln\left\{\frac{\Gamma(\delta+\mu+1)}{\Gamma(b+\mu+1)}\left[\frac{\Gamma(2b+\mu+1)}{\Gamma(\delta+\mu+1)}\right]^{\frac{b-\delta}{2b-\delta}}\right\}} \approx \sqrt{\frac{2}{b}\ln\left\{\frac{2\mu+2b+\delta+1}{2\mu+b+\delta+1}\right\}}\,. \qquad (52)$$

The constant line of the ratio = 1 in Fig. 10 satisfies the condition of Eq. (52). Therefore, the retrieved $r_{eff}$ from two algorithms are the same once 1) two algorithms use the same particle shape in terms of $a$, $b$, $\gamma$, and $\delta$, and 2) $\mu$ of the gamma PSD and $\omega$ of the lognormal PSD satisfy the Eq. (52). Otherwise, Eq. (51) should be applied for converting $r_{eff}$ derived with a gamma PSD into $r_{eff}$ derived with a lognormal PSD, or vice versa.

## 5.3. Conversion of $r_{eff}$ when different PSDs and particle shapes are used

In this section, we consider two algorithms that use different particle shapes and PSDs. Let us assume that $r_{eff,1}$ is retrieved from a set of coefficients $a_1$, $b_1$, $\gamma_1$, and $\delta_1$ and a gamma PSD, and $r_{eff,2}$ is retrieved from a set of coefficients $a_2$, $b_2$, $\gamma_2$, and $\delta_2$ and a lognormal PSD. Similar to Eq. (49), $Z/k_{ext}$ can be expressed with $r_{eff,1}$, $a_1$, $b_1$, $\gamma_1$, and $\delta_1$. Then $Z/k_{ext}$ in Eq. (41) is substituted with Eq. (49), and we obtain

$$r_{eff,2} = \frac{3}{4\rho_i}\frac{a_2}{\gamma_2}\left\{\frac{\pi^2\rho_i^2\gamma_2}{18 f_{Mie,2}a_2^2}\right\}^{\frac{b_2-\delta_2}{2b_2-\delta_2}} \exp\left(-\frac{b_2}{2}(b_2-\delta_2)\omega^2\right)\left\{\frac{Z}{k_{ext}}\right\}^{\frac{b_2-\delta_2}{2b_2-\delta_2}}$$

$$= \frac{3}{4\rho_i}\frac{a_2}{\gamma_2}\left\{\frac{a_1^2}{\gamma_1}\frac{\gamma_2}{a_2^2}\frac{f_{Mie,1}}{f_{Mie,2}}\right\}^{\frac{b_2-\delta_2}{2b_2-\delta_2}} \exp\left(-\frac{b_2}{2}(b_2-\delta_2)\omega^2\right)$$

$$\times\left\{r_{eff,1}\frac{4\rho_i\gamma_1}{3a_1}\frac{\Gamma(\delta_1+\mu+1)}{\Gamma(b_1+\mu+1)}\right\}^{\frac{2b_1-\delta_1}{b_1-\delta_1}\frac{b_2-\delta_2}{2b_2-\delta_2}}\left\{\frac{\Gamma(2b_1+\mu+1)}{\Gamma(\delta_1+\mu+1)}\right\}^{\frac{b_2-\delta_2}{2b_2-\delta_2}}. \qquad (53)$$

Equation (53) is a function of two sets of $a$, $b$, $\gamma$, and $\delta$, as well as $\mu$ and $\omega$. To simplify the relation in Eq. (53), we can use *priori* values of $\mu$ and $\omega$ that are used for $r_{eff}$ retrievals such as Eq. (31) or (47).

In Fig. 11, we consider two temperatures, −75°C, and −5°C, and compute $\mu$ using Eq. (31) and $\omega$ using (47). This corresponds to $\mu$ = 4.16 and −0.45, and $\omega$ = 0.21 and 0.66, respectively. We also assume in Fig. 11 that the same Mie correction factor is used in two algorithms ($f_{Mie,1} = f_{Mie,2}$). In Fig. 11, $r_{eff,1}$ is from m-D and A-D relationships of *Brown and Francis* (case (3) of Table 1) and a gamma PSD, while $r_{eff,2}$ is from other m-D and A-D relationships from Table 1 and a lognormal PSD. Compared to Fig. 9, two different temperatures produce significantly different relationships between $r_{eff,1}$ and $r_{eff,2}$. This is because of different dependencies of $\mu$ and $\omega$ on the temperature, i.e. Eq. (31) versus Eq. (47).

Deng et al. [2013] compared DARDAR with CloudSat 2B-CWC products, and they found that $r_{eff}$ from 2B-CWC is larger by 0−30% (see Fig. 7 of the reference). In Fig. 11, 2B-CWC corresponds to $r_{eff,2}$ using a spherical assumption (red line), and DARDAR corresponds to $r_{eff,1}$. When the temperature is −75°C, $r_{eff,2}$ with a spherical assumption is 30% larger than $r_{eff,1}$ (solid red line). In contrast, when the temperature is −5°C, $r_{eff,2}$ with a spherical assumption is 10% smaller than $r_{eff,1}$ (dashed red line). Therefore, a diverse range (0−30%) of differences between DARDAR and 2B-CWC found in Deng et al. [2013] can be explained by the range of temperature. Note that other factors influence the differences between DARDAR and 2B-CWC $r_{eff}$ because 2B-CWC uses radar only, while DARDAR uses radar and lidar. This study addresses the differences only caused by the assumption of particle shape and PSD. Equation (53) provides a possible conversion formula to overcome differences caused by particle shape and PSD assumptions.

## 6. Summary

This study analytically examines the impact of assumptions of ice particle shape on the effective radius derived from radar-lidar observations. We define the particle shape by four parameters, $a$, $b$, $\gamma$, and $\delta$, expressing the relationships between mass and maximum diameter (m-D), and projected area and maximum diameter (A-D). The m-D and A-D relationships are expressed using power laws for analytic integration of mass and projected area over the particle size distribution (PSD). We use gamma and lognormal PSDs in computing size-integrated optical properties such as radar reflectivity factor ($Z$), visible extinction coefficient ($k_{ext}$), effective radius ($r_{eff}$), and ice water content (IWC). Throughout the analysis, we assume that radar reflectivity factor and visible extinction are available, respectively, from radar and lidar measurements. We then express $r_{eff}$ and IWC as functions of four parameters used in the m-D and A-D relationships.

Different particle shape assumptions used in earlier studies lead to different m-D and A-D relationships (Fig. 1 and Table 1). This also results in a significant difference of mass-to-area ratio, which is directly related to the effective radius ($r_{eff}$) (Fig. 2). Among relationships examined in this study, the particle shape from Heymsfield et al. [2013] for $T = -60$°C gives the largest effective radius, while plates and bullets defined by Yang et al. [2000] give the smallest effective radius for a given $Z/k_{ext}$. These are obtained either we assume mono-disperse particles (Fig. 2) or a gamma PSD (Fig. 5).

Effects of $a$, $b$, $\gamma$, and $\delta$ on cloud retrievals are also quantified using the first-order derivatives. The signs of the derivatives for gamma (Eqs. (27−(30)) and lognormal (Eqs. (43)−(46)) PSDs are consistent. The results indicate that the effective radius increases with increasing $a$, decreasing $b$, decreasing $\gamma$, and increasing $\delta$. Altering $a$, $b$, $\gamma$, and $\delta$ by 10% changes $r_{eff}$ by more than 100% (Fig. 4). When we apply different m-D and A-D relationships shown in Table 1 (and thus different $a$, $b$, $\gamma$, and $\delta$), the largest $r_{eff}$ is almost twice as large as the smallest $r_{eff}$ (Fig. 5). The sensitivity of IWC to $a$, $b$, $\gamma$, and $\delta$ is the same to $r_{eff}$.

Because most radar-lidar inversion methods retrieve a larger number of unknown parameters than the number of equations that can be set up from measurements, they quite depend on *a priori* assumption of parameters in PSD. Therefore, we also examine how $r_{eff}$ is affected by the assumption of $\mu$ in gamma PSD. As $\mu$ increases, $r_{eff}$ also increases ($\partial(\ln r_{eff})/\partial\mu > 0$ in Eq. (32)). In addition, the sensitivity of $r_{eff}$ to $\mu$ increases with increasing $b$, decreasing $\delta$, or decreasing $\mu$ (magnitude of Eq. (32)). In contrast, $a$ and $\gamma$ do not change the sensitivity of $r_{eff}$ to $\mu$. When $\mu$ is increased by a factor of 2, $r_{eff}$ increases by 20−50% for $\mu < 0$, while $r_{eff}$ increases by < 10% for $\mu > 0$ (Fig. 6). We also examine effects of $\omega$ on $r_{eff}$ when a lognormal PSD is used. As $\omega$ increases, a smaller $r_{eff}$ is obtained ($\partial(\ln r_{eff})/\partial\omega < 0$ in Eq. (48)). The sensitivity of $r_{eff}$ to $\omega$ increases with increasing $\omega$, increasing $b$, or decreasing $\delta$ (magnitude of Eq. (48)). Among m-D and A-D relationships considered in this study, the particle shape of Heymsfield et al. [2013] at the temperature of −60°C shows the smallest dependence of $r_{eff}$ on $\mu$ and $\omega$, while the ice mixture by Yang et al. [2000] shows the largest dependence (Figs. 6 and 8).

We demonstrate the conversion method of $r_{eff}$ when different assumptions of particle shape and size distribution are used. First, we consider two retrieval algorithms that use the same gamma PSD, but assume different particle shapes, in terms of $a$, $b$, $\gamma$, and $\delta$. The effective radii derived from these two algorithms are related by Eq. (50). The relationship is a function of two sets of $a$, $b$, $\gamma$, and $\delta$ and dispersion parameter ($\mu$) of the gamma PSD. Different m-D and A-D relationships produce significant differences up to 100% in the retrieved $r_{eff}$ (Fig. 9).

Second, we consider two retrieval algorithms that use different PSDs, i.e. gamma and lognormal PSDs, but use the same particle shape ($a$, $b$, $\gamma$, and $\delta$). In this case, two values of $r_{eff}$ from the gamma and lognormal PSDs are related to each other by Eq. (51). The ratio of $r_{eff}$ depends on the dispersion parameter ($\mu$) of the gamma PSD and the width parameter ($\omega$) of the lognormal PSD (Fig. 10). When $\omega$ and $\mu$ are smaller (larger), a lognormal PSD leads to a larger (smaller) $r_{eff}$ than $r_{eff}$ derived with a gamma PSD (Fig. 10). The condition in which both PSDs derive the same $r_{eff}$ is given by Eq. (52).

Third, we consider two algorithms that use different PSDs and particle shapes. The relation of $r_{eff}$ is expressed with two sets of $a$, $b$, $\gamma$, $\delta$, $\mu$ of the gamma PSD, and $\omega$ of the lognormal PSD (Eq. (53)). We can simplify this relation using *a priori* $\mu$ and $\omega$ used for $r_{eff}$ retrievals. The relationship between two $r_{eff}$ from two algorithms depends on temperature because $\mu$ and $\omega$ have different dependencies on the temperature change.

Throughout this study, we assume that the Mie correction factor is independent of maximum dimension, and it is treated as a constant scaling factor when integrating the radar backscatter cross section over the particle size distribution (Eq. (8)). In addition, ice bulk density ($\rho_b$) is assumed to be the density of solid ice ($\rho_i$, 0.917 g $cm^{-3}$) (Eqs. (7), (8)), following Sato and Okamoto [2006]. Future studies are needed related to assumptions of the Mie scattering correction and ice bulk density.

Results of this study can be used to convert $r_{eff}$ derived with different particle shape and size distribution assumptions. Equations derived in this work provide an efficient way to avoid inconsistency between assumptions used in $r_{eff}$ retrievals and forward radiative transfer computations. Particle shape and PSD assumptions used in retrievals are not necessarily correct. Making the same assumptions in radiative transfer computations, however, eliminates the error caused by inconsistent assumptions.

## Acknowledgements

This work is supported by the Clouds and Earth's Radiant Energy System (CERES) and NASA Making Earth System Data Records for the Use in Research Environments (MEaSUREs) projects. The authors greatefully acknowledge three anonymous reviewers for their constructive and valuable comments. The authors would also like to thank Cooperative Institute for Research in the Atmosphere (CIRA) CloudSat Processing Data Center (DPC) for the CloudSat data (http://www.cloudsat.cira.colostate.edu) and Atmospheric Science Data Center (ASDC) for CALIPSO data (https://eosweb.larc.nasa.gov/).

## References

Atlas, D., S. Y. Matrosov, A. J. Heymsfield, M.-D. Chou, D. B. Wolff (1995), Radar and radiation properties of ice clouds, *J. Appl. Meteo.*, 34, 2329–2345.

Aumann, H. H., et al. (2003), AIRS/AMSU/HSB on the Aqua mission: Design, science objectives, data products, and processing systems, *IEEE Trans. Geosci. Remote Sens.*, 41, 253–264.

Austin, R. T., A. J. Heymsfield, and G. L. Stephens (2009), Retrieval of ice cloud microphysical parameters using the CloudSat millimeter-wave radar and temperature, *J. Geophys. Res.*, 114, D00A23, doi: 10.1029/2008JD010049.

Battaglia, A., M. O. Ajewole, and C. Simmer (2005), Multiple scattering effects due to hydrometeors on precipitation radar systems, *Geophys. Res. Lett.*, 32, L19801, doi: 10.1029/2005GL023810.

Battaglia, A., M. O. Ajewole, and C. Simmer (2007), Evaluation of radar multiple scattering effects in CloudSat configuration, *Atmos. Chem. Phys.*, 7, 1719–1730.

Baum, B. A., A. J. Heymsfield, P. Yang, and S. T. Bedka (2005a), Bulk scattering properties for the remote sensing of ice clouds. Part I: Microphysical data and models, *J. Appl. Meteor.*, 44, 1885–1895.

Baum, B. A., P. Yang, A. J. Heymsfield, S. Platnick, M. D. King, Y.-X. Hu, and S. T. Bedka (2005b), Bulk scattering properties for the remote sensing of ice clouds. Part II: Narrowband models, *J. Appl. Meteor.*, 44, 1896–1911.

Benedetti, A., G. L. Stephens, and J. M. Haynes (2003), Ice cloud microphysics retrievals from millimeter radar and visible optical depth using an estimation theory approach, *J. Geophys. Res.*, 108(D11), 4335, doi: 10.1029/2002JD002693.

Bouldala, F., G. A. Isaac, Q. Fu, S. G. Cober (2002), Parameterization of effective ice particle size for high-latitude clouds, *Int. J. Climatol.*, 22, 1267–1284, doi: 10.1002/joc.774.

Brown, P. R. A., and P. N. Francis (1995), Improved measurements of the ice water content in cirrus using a total-water probe, *J. Atmos. Ocean. Tech.*, 12, 410–414.

Brown, P. R., A. J. Illingnorth, A. J. Heymsfield, G. M. McFarquhar, K. A. Browning, and M. Gosset (1995), The role of spaceborne millimeter-wave radar in the global monitoring of ice cloud, *J. Appl. Meteo.*, 34, 2346–2366.

Burić, T. and N. Elezović (2011), Bernoulli polynomials and asymptotic expansions of the quotient of gamma functions, *J. Comput. Appl. Math.*, 235 (11), 3315–3331.

Burton, S. P., R. A. Ferrare, C. A. Hostetler, J. W. Hair, R. R. Rogers, M. D. Obland, C. F. Butler, A. L. Cook, D. B. Harper, and K. D. Froyd (2012), Aerosol classification using airborne High Spectral Resolution Lidar measurements - methodology and examples, *Atmos. Meas. Tech.*, 5, 73-98, doi: 10.5194/amt-5-73-2012.

Delanoë, J. and R. J. Hogan (2008), A variational scheme for retrieving ice cloud properties from combined radar, lidar and infrared radiometer, *J. Geophys. Res.*, 113, D07204, doi: 10.1029/2007JD009000.

Delanoë, J. and R. J. Hogan (2010), Combined CloudSat-CALIPSO-MODIS retrievals of the properties of ice clouds, *J. Geophys. Res.*, 115, D00H29, doi: 10.1029/2009JD012346.

Deng, M., G. G. Mace, Z. Wang, and H. Okamoto (2010), Tropical composition, cloud and climate coupling experiment validation for cirrus cloud profiling retrieval using CloudSat radar and CALIPSO lidar, *J. Geophys. Res.*, 115, D00J15, doi: 10.1029/2009JD013104.

Deng, M., G. G. Mace, Z. Wang, R. P. Lawson (2013), Evaluation of several A-Train ice cloud retrieval products with in situ measurements collected during the SPARTICUS Campaign, *J. Appl. Meteo. Clim.*, 52, 1014–1030.

Deng, M., G. G. Mace, Z. Wang, and E. Berry (2015), CloudSat 2C-ICE product update with a new Ze parameterization in lidar-only region, *J. Geophys. Res.*, 120, 12,198–12,208, doi:10.1002/2015JD023600.

Donovan, D. P. and A. C. A. P. Van Lammeren (2001), Cloud effective size and water content profile retrievals using combined lidar and radar observations. 1. Theory and examples, *J. Geophy. Res.*, 106, 27 425–27 448.

Erfani, E. and D. Mitchell (2016), Developing and bounding ice particle mass- and area-dimension, *Atmos. Chem. Phys.,* 16, 4379–4400, doi: 10.5194/acp-16-4379-2016.

Field, P. R., A. J. Heymsfield, and A. Bansemer (2006), Shattering and particle interarrival times measured by optical array probes in ice clouds, *J. Atmos. Ocean. Tech.*, 23, 1357–1371, doi: 10.1175/JTECH1922.1.

Fontaine, E., A. Schwarzenboeck, J. Delanoë, W. Wobrock, D. Leroy, R. Dupuy, C. Gourbeyre, and A. Protat (2014), Constraining mass–diameter relations from hydrometeor images and cloud radar reflectivities in tropical continental and oceanic convective anvils, *Atmos. Chem. Phys.*, 14, 11 367–11 392, doi: 10.5194/acp-14-11367-2014.

Foot, J. S. (1988), Some observations of the optical properties of clouds—2. Cirrus, *Quart. J. Roy. Meteor. Soc.*, 114, 145–164.

Francis, P. N., P. Hignett, and A. Macke (1998), The retrieval of cirrus cloud properties from aircraft multi-spectral reflectance measurements during EUCREX'93, *Quart. J. Roy. Meteor. Soc.*, 124, 1273–1291.

Garnier, A., J. Pelon, M. A. Vaughan, D. M. Winker, C. R. Trepte, and P. Dubuisson (2015), Lidar multiple scattering factors inferred from CALIPSO lidar and IIR retrievals of semi-transparent cirrus cloud optical depths over oceans, *Atmos. Meas. Tech.*, 8, 2759–2774.

Haarig, M., R. Engelmann, A. Ansmann, I. Veselovskii, D. N. Whiteman, and D. Althausen (2016), 1064 nm rotational Raman lidar for particle extinction and lidar-ratio profiling: cirrus case study, *Atmos. Meas. Tech.*, 9, 4269–4278, doi: 10.5194/amt-9-4269-2016.

Hammonds, K. D., G. G. Mace, and S. Y. Matrosov (2014), Characterizing the Radar Backscatter-Cross-Section Sensitivities of Ice-Phase Hydrometeor Size

Distributions via a Simple Scaling of the Clausius–Mossotti Factor, J. Appl. Meteo. Clim., 53, 2761–2774, DOI: 10.1175/JAMC-D-13-0280.1.

Heymsfield, A. J., A. Bansemer, P. R. Field, S. L. Durden, J. L. Stith, J. E. Dye, W. Hall, C. A. Grainger (2002), Observations and parameterizations of particle size distributions in deep tropical cirrus and stratiform precipitating clouds: Results from in situ observations in TRMM field campaign, *J. Atmos. Sci.*, 59, 3457–3491.

Heymsfield, A. J., A. R. Bansemer, C. G. Schmitt, C. H. Twohy, M. Poellot (2004), Effective ice particle densities derived from aircraft data, *J. Atmos. Sci.*, 61, 982–1003.

Heymsfield, A. J., C. Schmitt, and A. Bansemer (2013), Ice cloud particle size distributions and pressure-dependent terminal velocities from in situ observations at temperatures from 0° to −86°C, *J. Atmos. Sci.*, 70, 4123–4154, doi: 10.1175/JAS-D-12-0124.1

Hogan, R. J., P. R. Field, A. J. Illingworth, R. J. Cotton, and T. W. Choularton (2002), Properties of embedded convection in warm-frontal mixed-phase cloud from aircraft and polarimetric radar, *Q. J. R. Meteorol. Soc.*, 128, 451–476.

Hogan, R. J., D. P. Donovan, C. Tinel, M. E. Brooks, D. Bouniol, A. J. Illingworth, and J. P. V. P. Baptista (2006a), Independent evaluation of the ability of spaceborne radar and lidar to retrieve the microphysical and radiative properties of ice clouds, *J. Atmos. Oceanic Tech.*, 23, 211–227.

Hogan, R. J., M. P. Mittermaier, and A. J. Illingworth (2006b), The retrieval of ice water content from radar reflectivity factor and temperature and its use in evaluating a mesoscale model, *J. Appl. Meteo. Clim.*, 45, 301–317.

Holz, R. E., S. Platnick, K. Meyer, M. Vaughan4, A. Heidinger, P. Yang, G. Wind, S. Dutcher, S. Ackerman, N. Amarasinghe, F. Nagle, and C. Wang (2016), Resolving ice cloud optical thickness biases between CALIOP and MODIS using infrared retrievals, *Atmos. Chem. Phys.*, 16, 5075–5090.

Hou, T., H. Lei, Z. Hu, and J. Zhou (2014), Aircraft observations of ice particle properties in stratiform precipitating clouds, *Adv. Meteo.*, doi: 10.1155/2014/206352.

Kienast-Sjögren, E., C. Rolf, P. Seifert, U. K. Krieger, B. P. Luo, M. Krämer, and T. Peter (2016), Climatological and radiative properties of midlatitude cirrus clouds derived by automatic evaluation of lidar measurements, *Atmos. Chem. Phys.*, 16, 7605–7621, doi:10.5194/acp-16-7605-2016.

Kosarev, A. L. and I. P. Mazin (1991), An empirical model of the physical structure of upper layer clouds, *Atmos. Res.*, 26, 213–228.

Korolev, A. and R. R. Field (2015), Assessment of the performance of the inter-arrival time algorithm to identify ice shattering artifacts in cloud particle probe measurements, *Atmos. Meas. Tech.*, 8, 761-777, doi:10.5194/amt-8-761-2015.

Lawson, R. P., D. O'conner, P. Zmarzly, K. Weaver, B. Baker, Q. Mo, and H. Jonsson (2006), The 2D-S (Stereo) Probe: Design and Preliminary Tests of a New Airborne, High-Speed, High-Resolution Particle Imaging Probe, *J. Atmos. Ocean. Tech.*, 23, 1462–1477, doi: 10.1175/JTECH1927.1.

Lawson, R. P. (2011), Effects of ice particles shattering on the 2D-S probe, *Atmos. Meas. Tech.*, 4, 1361–1381.

Lebsock, M. (2011), Level 2C RAIN-PROFILE Product Process Description and Interface Control Document Algorithm version 0.0, 20 June 2011, CloudSat Project, available at http://www.cloudsat.cira.colostate.edu/sites/default/files/products/ files/ 2C-RAIN-PROFILE-PDICD.P_R04.20110620.pdf.

Mace, G. G. and S. Benson (2017), Diagnosing Cloud Microphysical Process Information from Remote Sensing Measurements; A Feasibility Study Using Aircraft Data. Part I: Tropical Anvils Measured during TC4, J. Appl. Meteo. Climatol., in press.

Marchand, R., G. G. Mace, T. Ackerman, and G. Stephens (2008), Hydrometeor detection using CloudSat – An Earth-orbiting 94-GHz Cloud radar, *J. Atmos. Ocean. Tech.*, 25, 519–533, doi: 10.1175/2007JTECHA1006.1.

McFarlane, S. and K. F. Evans (2004), Clouds and shortwave fluxes at Nauru. Part I: Retrieved cloud properties, *J. Atmos. Sci.*, 61, 733–744.

McFarquhar, G. M., M. S. Timlin, R. M. Rauber, B. F. Jewett, J. A. Grim, and D. P. Jorgensen (2007), Vertical variability of cloud hydrometeors in the stratiform region of mesoscale convective systems and bow echoes, *Mon. Weather Rev.*, 135, 3405–3428, doi:10.1175/MWR3444.1.

Mitchell, D. L. (1991), Evolution of snow-size spectra in cyclonic storms. Part II: Deviations from the exponential form, *J. Atmos. Sci.*, 48, 1885–1899.

Mitchell, D. L. (1996), Use of mass- and area-dimensional power laws for detecting precipitation particle terminal velocities, *J. Atmos. Sci.*, 53(12), 1710–1723.

Mitchell, D. L., A. Macke, and Y. Liu (1996), Modeling cirrus clouds. Part II: Treatment of radiative properties, *J. Atmos. Sci.*, 53, 2967–2988.

Myagkov, A., P. Seifert, U. Wandinger, J. Bühl, J., and R. Engelmann (2016), Relationship between temperature and apparent shape of pristine ice crystals derived from polarimetric cloud radar observations during the ACCEPT campaign, *Atmos. Meas. Tech.*, 9, 3739-3754, doi:10.5194/amt-9-3739-2016.

Okamoto, H., S. Iwasaki, M. Yasui, H. Horie, H. Kuroiwa, and H. Kumagai (2003), An algorithm for retrieval of cloud microphysics using 95-GHz cloud radar and lidar, *J. Geophys. Res.*, 108, 4226–4247.

Olver, F. W. J., D. W. Lozier, R. F. Boisvert, and C. W. Clark, editors. *NIST Handbook of Mathematical Functions*. Cambridge University Press, New York, NY, 2010. Print companion to http://dlmf.nist.gov/, Release 1.0.10.

Patade, S., T. V. Prabha, D. Axisa, K. Gayatri, and A. Heymsfield (2015), Particle size distribution properties in mixed-phase monsoon clouds from in situ measurements during CAIPEEX, *J. Geophys. Res.*, 120, 10 418–10 440, doi:10.1002/2015JD023375.

Platt, C. (1979), Remote sounding of high clouds: I. Calculation of visible and infrared optical properties from lidar and ratiometer measurements, *J. Appl. Meteo.*, 18, 1130–1143.

Platt, C. M., D. M. Winker, M. A. Vaughan, and S. D. Miller (1998), Backscatter-to-extinction ratios in the top layers of tropical mesoscale convective systems and isolated cirrus from LITE observations, *J. Appl. Meteo.*, 38, 1330–1345.

Rienecker, M. M., et al. (2011), MERRA: NASA’s Modern-Era Retrospective Analysis for Research and Application, *J. Clim.*, 24, 3624–3648, doi: 10.1175/JCLI-D-11-00015.1.

Sato, K. and H. Okamoto (2006), Characterization of $Z_e$ and LDR of nonspherical and inhomogeneous ice particles for 95-GHz cloud radar: Its implication to microphysical retrievals, *J. Geophy. Res.*, 111, D22213, doi:10.1029/2005JD006959

Schneider, T. and G. L. Stephens (1995), Theoretical aspects of modeling backscattering by cirrus ice particles at millimeter wavelengths, *J. Atmos. Sci.*, 52(23), 4367–4385.

Seifert, P., A. Ansmann, D. Müller, U. Wandinger, D. Althausen, A. J. Heymsfield, S. T. Massie, and C. Schmitt (2007), Cirrus optical properties observed with lidar, radiosonde, and satellite over the tropical Indian Ocean during the aerosol-polluted northeast and clean maritime southwest monsoon, *J. Geophys. Res.*, 112, D17205, doi:10.1029/2006JD008352.

Smith, P. (1984), Equivalent radar reflectivity factors for snow and ice particles, *J. Clim. Appl. Meteo.*, 23, 1258–1260.

Stein, T. M., J. Delanoë, and R. J. Hogan (2011), A comparison between four different retrieval methods for ice cloud prop- erties using data from CloudSat, CALIPSO, and MODIS, *J. Appl. Meteor. Climatol.*, 50, 1952–1969.

Stephens, G. L., et al. (2002), The Cloudsat Mission and the A-Train, *Bull. Amer. Meteor. Soc.*, 83, 1771–1790.

Stephens, G. L., et al. (2008), CloudSat mission: Performance and earlyscience after the first year of operation, *J. Geophys. Res.*, 113, 00A18, doi:10.1029/2008JD009982.

Tian, L., G. M. Heymsfield, A. J. Heymsfield, A. Bansemer, L. Li, C. H. Twohy, and R. C. Srivastava (2010), A study of cirrus ice particle size distribution using TC4 observations, *J. Atmos. Sci.*, 67, 195–216.

Tinel, C., J. Testud, R. J. Hogan, A. Protat, J. Delanoë, and D. Bouniol (2005), The retrieval of ice cloud properties from cloud radar and lidar synergy, *J. Appl. Meteor.*, 44, 860–875.

Tobin, D. C., H. E. Revercomb, R. O. Knuteson, B. M. Lesht, L. L. Strow, S. E. Hannon, W. F. Feltz, L. A. Moy, E. J. Fetzer, and T. S. Cress (2006), Atmospheric Radiation Measurement site atmospheric state best estimates for Atmospheric

Infrared Sounder temperature and water vapor retrieval validation, *J. Geophys. Res.*, 111, D09S14, doi:10.1029/2005JD006103.

Um, J., G. M. McFarquhar, Y. P. Hong, S-S Lee, C. H. Jung, R. P. Lawson, and Q. Mo (2015), Dimensions and aspect ratios of natural ice crystals, *Atmos. Chem. Phys.*, 15, 3933–3956.

Whiteman, D. N., B. Demoz, and Z. Wang (2004), Subtropical cirrus cloud extinction to backscatter ratios measured by Raman Lidar during CAMEX-3, *Geophys. Res. Lett.*, 31, L12105, doi:10.1029/2004GL020003.

Winker, D. M., J. Pelon, and M. P. McCormick (2003), The CALIPSO mission: Spaceborne lidar for observation of aerosols and clouds. Lidar Remote Sensing for Industry and Environment Monitoring III, U. N. Singh, T. Itabe, and Z. Liu, Eds., International Society for Optical Engineering, *SPIE Proceedings*, Vol. 4893, 1–11.

Winker, D. M., M. A. Vaughan, A. Omar, Y.-X. Hu, K. A. Powell, Z. Liu, W. H. Hunt, and S. A. Young (2009), Overview of the CALIPSO mission and CALIOP data processing algorithms, *J. Atmos. Ocean. Tech.*, 26, 2310–2323.

Yang, P., K. Liou, K. Wyser, and D. Mitchell (2000), Parameterization of the scattering and absorption 25 properties of individual ice crystals, *J. Geophys. Res.*, 105, 4699–4718.

Young, S. A. and M. A. Vaughan (2009), The retrieval of profiles of particulate extinction from Cloud-Aerosol Lidar Infrared Pathfinder Satellite Observations (CALIPSO) data: Algorithm description, *J. Atmos. Ocean. Tech.*, 26, 1105–1119.

## Appendix A: Error analysis of the asymptotic theory for a ratio of two gamma functions

According to Burić and Elezović [2011] and Olver et al. [2010],

$$\left(\frac{\Gamma(\mathrm{x}+\mathrm{p})}{\Gamma(\mathrm{x}+\mathrm{q})}\right)^{\frac{1}{p-q}} \sim \mathrm{x} + f_0 + \frac{1}{\mathrm{x}} f_1 + \frac{1}{\mathrm{x}^2} f_2 + \frac{1}{\mathrm{x}^3} f_3 + \frac{1}{\mathrm{x}^4} f_4 + o(\mathrm{x}^{-5}) \;, \tag{A1}$$

where

$$f_0(p,q) = \frac{p+q-1}{2} \;, \tag{A2}$$

$$f_1(p,q) = \frac{1}{24}[1-(p-q)^2] \;, \tag{A3}$$

$$f_2(p,q) = -f_0 f_1 \;, \tag{A4}$$

$$f_3(p,q) = \frac{f_1}{10}\left(10{f_0}^2 - 13 f_1 - 1\right) \text{, and} \tag{A5}$$

$$f_4(p,q) = \frac{-f_0 f_1}{10}\left(10{f_0}^2 - 39 f_1 - 3\right) . \tag{A6}$$

To apply the asymptotic theory to $\Gamma(b+\mu+1)/\Gamma(\delta+\mu+1)$ in Eq. (23), we define

$$x = \mu + \delta + 1 \;, \tag{A7}$$

$$p = b - \delta \text{, and} \tag{A8}$$

$$q = 0 \;. \tag{A9}$$

Then Eq. (A1) can be expressed as

$$\left(\frac{\Gamma(\mu+\mathrm{b}+1)}{\Gamma(\mu+\delta+1)}\right)^{\frac{1}{b-\delta}} \cong (\mu+\delta+1) + f_0 + \frac{1}{\mu+\delta+1} f_1 + \frac{1}{(\mu+\delta+1)^2} f_2 + \frac{1}{(\mu+\delta+1)^3} f_3$$

$$+ \frac{1}{(\mu+\delta+1)^4} f_4 + o((\mu+\delta+1)^{-5}) \;. \tag{A10}$$

Regarding $p - q = b - \delta$, Eqs. (A2)− (A6) become

$$f_0(b,\delta) = \frac{b-\delta-1}{2} , \tag{A11}$$

$$f_1(b,\delta) = \frac{1}{24}[1-(b-\delta)^2] \;, \tag{A12}$$

$$f_2(b,\delta) = -f_0 f_1 \;, \tag{A13}$$

$$f_3(b,\delta) = \frac{f_1}{10}\left(10{f_0}^2 - 13 f_1 - 1\right) \text{, and} \tag{A14}$$

$$f_4(b,\delta) = \frac{-f_0 f_1}{10}\left(10{f_0}^2 - 39 f_1 - 3\right) . \tag{A15}$$

As $\mu + \delta + 1$ increases, the high-order terms converge to zero in Eq. (A10), and the equation can be approximated with a few terms. In other words, when $\mu + \delta + 1$ has the minimum value, ignoring the high-order terms leads the maximum uncertainty in Eq. (A10). According to in-situ measurements [Heymsfield et al., 2002, 2013; Patade et al., 2015; Hou et al., 2014], $\mu$ is typically from −2 to 10, and thus the minimum of $\mu + \delta + 1$ can be considered as $\delta - 1$. Table (A1) provides the magnitude of each term when the minimum value of $\mu + \delta + 1$ (= $\delta - 1$) is used. The sum of the first (= $\mu_{min} + \delta + 1$) and second (= $f_0$) terms is > 98%, > 95%, > 99%, > 96%, and 100% of the true values of (A10), when $a$, $b$, $\gamma$, and $\delta$ are from *Brown and Francis*, plates of Yang et al. [2000], solid columns of Yang et al. [2000], ice mixtures of Yang et al. [2000], and spherical particles, respectively. This means that we can ignore the terms higher than the third orders with a less than 5% uncertainty for these m-D and A-D relationships. Neglecting terms higher than the third orders, Eq. (A10) can be approximated as

$$\left(\frac{\Gamma(\mu+b+1)}{\Gamma(\mu+\delta+1)}\right)^{\frac{1}{b-\delta}} \cong (\mu+\delta+1)+\frac{b-\delta-1}{2} = \mu+\frac{b+\delta+1}{2} . \qquad \text{(A16)}$$

In a similar way, we can define $x$, $p$, and $q$ for the approximation of $\Gamma(2b + \mu + 1)/\Gamma(\delta + \mu + 1)$ in the last term of Eq. (23), as follows:

$$x = \mu + \delta + 1 , \qquad \text{(A17)}$$

$$p = 2b - \delta \text{ , and} \qquad \text{(A18)}$$

$$q = 0 . \qquad \text{(A19)}$$

Then we get

$$\left(\frac{\Gamma(\mu+2b+1)}{\Gamma(\mu+\delta+1)}\right)^{\frac{1}{2b-\delta}} \cong (\mu+\delta+1)+f_0+\frac{1}{\mu+\delta+1}f_1+\frac{1}{(\mu+\delta+1)^2}f_2+\frac{1}{(\mu+\delta+1)^3}f_3$$
$$+\frac{1}{(\mu+\delta+1)^4}f_4+o((\mu+\delta+1)^{-5}) . \qquad \text{(A20)}$$

Table A2 lists the magnitude of each term in Eq. (A20). The sum of the first (= $\mu_{\min} + \delta + 1$) and second (= $f_0$) terms is larger than the true value of (A20), and the difference is 12–16%. This means that the approximation in Eq. (A20) has a larger uncertainty than the approximation in Eq. (A10). However, $\Gamma(2b + \mu + 1)/\Gamma(\delta + \mu + 1)$ has a smaller exponent [= $(b - \delta)/(2b - \delta)$] than that (=1) of $\Gamma(b + \mu + 1)/\Gamma(\delta + \mu + 1)$ in Eq. (23). As a result, the approximation of $\Gamma(2b + \mu + 1)/\Gamma(\delta + \mu + 1)$ introduces a relatively smaller uncertainty, compared to the approximation of $\Gamma(b + \mu + 1)/\Gamma(\delta + \mu + 1)$ in Eq. (23).

To estimate total uncertainties by approximating $\Gamma(b + \mu + 1)/\Gamma(\delta + \mu + 1)$ and $\Gamma(2b + \mu + 1)/\Gamma(\delta + \mu + 1)$ in Eq. (23), we get the ratio as

$$\frac{R_{approx}-R_{true}}{R_{true}} \times 100\% \,, \tag{A21}$$

where

$$R_{true} = \frac{\Gamma(b+\mu+1)}{\Gamma(\delta+\mu+1)} \left\{ \frac{\Gamma(\delta+\mu+1)}{\Gamma(2b+\mu+1)} \right\}^{(b-\delta)/(2b-\delta)} \quad \text{and} \tag{A22}$$

$$R_{approx} = \left\{ \mu + \frac{b+\delta+1}{2} \right\}^{b-\delta} \left\{ \mu + \frac{2b+\delta+1}{2} \right\}^{-b+\delta} . \tag{A23}$$

Note that Eqs. (A22) and (A23) are used in Eqs. (23) and (25), respectively. In Fig. A1, $(R_{approx} - R_{true})/R_{true} \times 100\%$ is over 10% when $\mu = -2$. The error rapidly decreases with increasing $\mu$, and the error is $< 2\%$ for $\mu > 2$.

## Appendix B: Slopes of constant lines of $r_{eff}$ and $Z/k_{ext}$ in a $\mu$-$\Lambda$ domain

In Section 3.2, we discuss that a unique solution of $N_0$, $\mu$, and $\Lambda$ does not exist because the number of equations is smaller than the number of unknown parameters. Figure B1 further demonstrates that we cannot obtain a unique solution of $r_{eff}$ from observed $Z/k_{ext}$, as a result of multiple solutions of $N_0$, $\mu$, and $\Lambda$. In Figs. B1a and B1b, constant lines of $r_{eff}$ and $Z/k_{ext}$ are drawn in a $\mu$-$\Lambda$ domain, respectively. The m-D and A-D relationships are computed using *Brown and Francis* (case (3) of Table 1). Note that the lidar and radar measurements provide a value of $Z/k_{ext}$, and solutions of $\mu$ and $\Lambda$ exist along the constant line of $Z/k_{ext}$. If the contour lines of $r_{eff}$ and $Z/k_{ext}$ in Fig. B1 overlay in the $\mu$-$\Lambda$ domain, we get a single solution of $r_{eff}$ for the given $Z/k_{ext}$. The slopes and intercepts of the constant lines of $r_{eff}$ and $Z/k_{ext}$ in Fig. B1 can be derived as follows. First, Eq. (20) can be rewritten as

$$\Lambda^{b-\delta} = \left( \frac{1}{r_{eff}} \frac{3a}{4\rho_i\gamma} \right) \frac{\Gamma(b+\mu+1)}{\Gamma(\delta+\mu+1)} \,. \tag{B1}$$

Using Eq. (24), Eq. (B1) can be approximated as

$$\Lambda = \left( \frac{1}{r_{eff}} \frac{3a}{4\rho_i\gamma} \right)^{\frac{1}{b-\delta}} \left( \mu + \frac{b+\delta+1}{2} \right) . \tag{B2}$$

Equation (B2) is represented as $\Lambda = A_0\,(\mu - A_1)$ where

$$A_0 = \left( \frac{1}{r_{eff}} \frac{3a}{4\rho_i\gamma} \right)^{\frac{1}{b-\delta}} \quad \text{and} \tag{B3}$$

$$A_1 = -\frac{b+\delta+1}{2} \,. \tag{B4}$$

Therefore, a constant line of $r_{eff}$ has $A_0$ as a slope, and $A_1$ as a $\mu$-intercept in the $\mu$-$\Lambda$ domain (Fig. B1a). In the same way, Eq. (21) can be rewritten as

$$\Lambda = \left(\frac{k_{ext}}{Z}\frac{18 f_{Mie} a^2}{\pi^2 \rho_i^2 \gamma}\right)^{\frac{1}{2b-\delta}} \left(\frac{\Gamma(2b+\mu+1)}{\Gamma(\delta+\mu+1)}\right)^{\frac{1}{2b-\delta}} . \quad \text{(B5)}$$

Using Eq. (24), Eq. (B5) is approximated as

$$\Lambda = \left(\frac{k_{ext}}{Z}\frac{18 f_{Mie} a^2}{\pi^2 \rho_i^2 \gamma}\right)^{\frac{1}{2b-\delta}} \left(\mu + \frac{(2b+\delta+1)}{2}\right) . \quad \text{(B6)}$$

Equation (B6) can be represented as $\Lambda = B_0\,(\mu - B_1)$ where

$$B_0 = \left(\frac{k_{ext}}{Z}\frac{18 f_{Mie} a^2}{\pi^2 \rho_i^2 \gamma}\right)^{\frac{1}{2b-\delta}} \text{ and} \quad \text{(B7)}$$

$$B_1 = -\frac{(2b+\delta+1)}{2} . \quad \text{(B8)}$$

Above indicates that a constant line of $Z/k_{ext}$ has $B_0$ as a slope, and $B_1$ as a $\mu$-offset in the $\mu$-$\Lambda$ domain (Fig. B1b). Note that $|A_1| \le |B_1|$ by comparing between Eqs. (B4) and (B8). Therefore, a constant line of $Z/k_{ext}$ has a larger $\mu$-offset than $r_{eff}$ in the $\mu$-$\Lambda$ domain, as also shown in Fig. B1. In addition, by rearranging Eq. (25),

$$\left(\frac{k_{ext}}{Z}\frac{18 f_{Mie}}{\pi^2 \rho_i^2}\frac{a^2}{\gamma}\right)^{\frac{1}{2b-\delta}} = \left(\frac{3a}{4\rho_i \gamma}\frac{1}{r_{eff}}\right)^{\frac{1}{b-\delta}} \left(\frac{2\mu+b+\delta+1}{2\mu+2b+\delta+1}\right)^{\frac{1}{b-\delta}} . \quad \text{(B9)}$$

Combining Eqs. (B3), (B7), and (B9), we get

$$B_0 = A_0 \left(\frac{2\mu+b+\delta+1}{2\mu+2b+\delta+1}\right)^{\frac{1}{b-\delta}} . \quad \text{(B10)}$$

For $b \neq 0$ and $b \neq \delta$, $\left(\frac{2\mu+b+\delta+1}{2\mu+2b+\delta+1}\right)^{\frac{1}{b-\delta}} < 1$, and thus $A_0 > B_0$ in Eq. (B10). Therefore, a slope of the constant line of $r_{eff}$ is larger than that of $Z/k_{ext}$, which is also found in Fig. B1.

If $b = \delta$, $r_{eff} = 3a/(4\,\rho_i\,\gamma)$ from Eq. (23). In this case, $r_{eff}$ is constant regardless of the choice of $\mu$ and $\Lambda$, which is the same condition for Eq. (32) = $\partial(\ln r_{eff})/\partial\mu = 0$ or Eq. (48) = $\partial(\ln r_{eff})/\partial\omega = 0$. For $b = 0$, $A_1 = B_1$ from Eqs. (B4) and (B8). Also $A_0 = B_0$ from Eq. (B10). This means that $r_{eff}$ and $Z/k_{ext}$ have the same slope and offset, and $r_{eff}$ has a single solution for the given $Z/k_{ext}$, regardless of the choice of $\mu$ and $\Lambda$. This is also consistent with Eq. (32) = 0 or Eq. (48) = 0. However, the ideal case of $b = 0$ or $b = \delta$ would not practically happen, because mass increases with the maximum dimension ($b > 0$), and also mass increases faster than projected area with the maximum dimension ($b > \delta$).

Table 1. Coefficients ($a$, $b$, $\gamma$, and $\delta$) of m-D and A-D relationships derived in earlier studies. All variables are in cgs units; $D$ in cm, $m(D)$ in gram, and $A(D)$ in cm$^2$. Small $D$ for Brown Francis corresponds to $D < 97 \times 10^{-4}$ cm for $m(D)$, and $D < 128 \times 10^{-4}$ cm for $A(D)$. Large $D$ for Brown and Francis corresponds to $D \geq 97 \times 10^{-4}$ cm for $m(D)$, and $D \geq 128 \times 10^{-4}$ cm for $A(D)$.

| | Ice habit/shape | $m(D) = aD^b$ | | $A(D) = \gamma D^\delta$ | | Case Number |
|---|---|---|---|---|---|---|
| | | $a$ (g cm$^{-b}$) | $b$ (unitless) | $\gamma$ (g cm$^{2-\delta}$) | $\delta$ (unitless) | |
| Brown and Francis [1995] and Francis et al. [1998] | Small $D$ | 0.480140 | 3.00000 | 0.785398 | 2.00000 | (1) |
| | Large $D$ | 0.002938 | 1.90000 | 0.026240 | 1.26667 | (2) |
| | All $D$ | 0.145666 | 2.80290 | 0.650146 | 1.96859 | (3) |
| Heymsfield et al. [2013] | $T = -30$°C | 0.005484 | 2.14800 | 0.116804 | 1.61407 | (4) |
| | $T = -45$°C | 0.004513 | 2.06700 | 0.106844 | 1.60273 | (5) |
| | $T = -60$°C | 0.003713 | 1.98600 | 0.125475 | 1.64494 | (6) |
| Yang et al. [2000] | Plate | 0.008210 | 2.44908 | 0.159987 | 1.77561 | (7) |
| | Solid Column | 0.086534 | 2.77712 | 0.313698 | 1.86699 | (8) |
| | Bullet-6 | 0.004834 | 2.50649 | 0.076765 | 1.71809 | (9) |
| | Mixture | 0.497345 | 3.29561 | 0.847120 | 2.14675 | (10) |
| Sphere | | 0.480140 | 3.00000 | 0.785398 | 2.00000 | (11) |

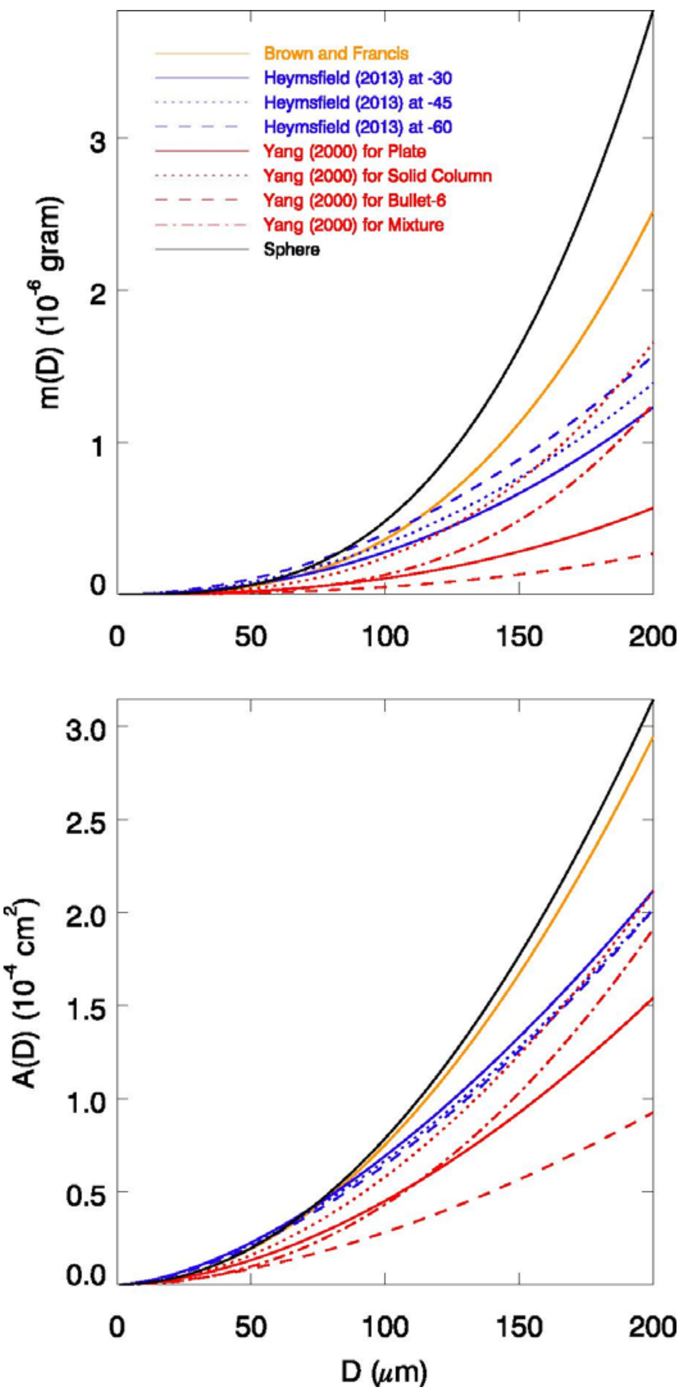


Figure 1. Mass [$m(D)$] and projected area [$A(D)$] as a function of diameter (maximum linear dimension, $D$). Different lines represent nine sets of $a$, $b$, $\gamma$, and $\delta$ provided by cases (3)–(11) of Table 1.

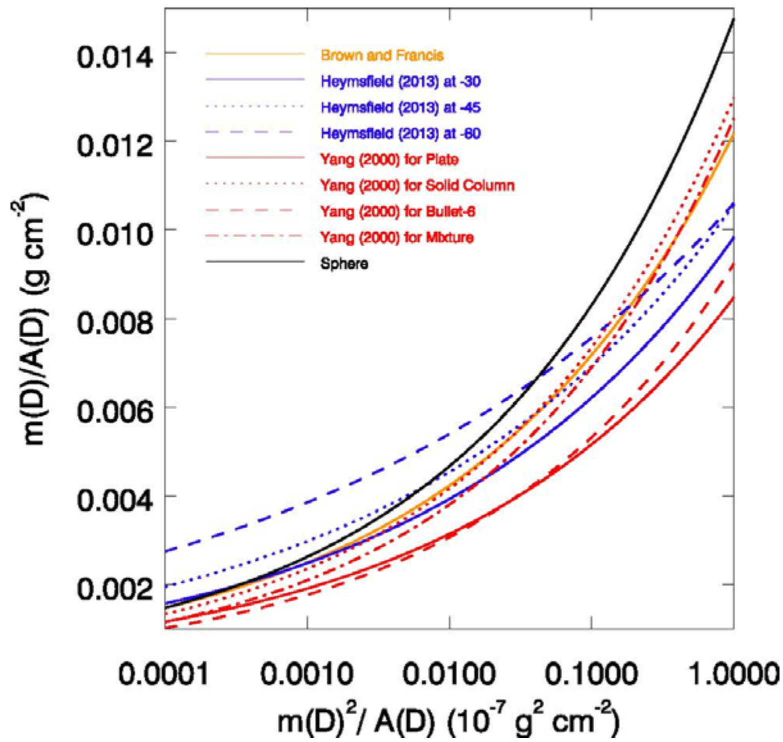


Figure 2. Relationships between $m(D)^2/A(D)$ and $m(D)/A(D)$. The radar-reflectivity-to-extinction-ratio with a particle size $D$ is proportional to $m(D)^2/A(D)$, while the effective radius is proportional to $m(D)/A(D)$. Therefore, the relationship between $m(D)^2/A(D)$ and $m(D)/A(D)$ approximately equals to the relationship between radar-reflectivity-to-extinction-ratio and effective radius for a particle size $D$. Different lines represent nine sets of $a$, $b$, $\gamma$, and $\delta$ provided by cases (3)–(11) of Table 1.

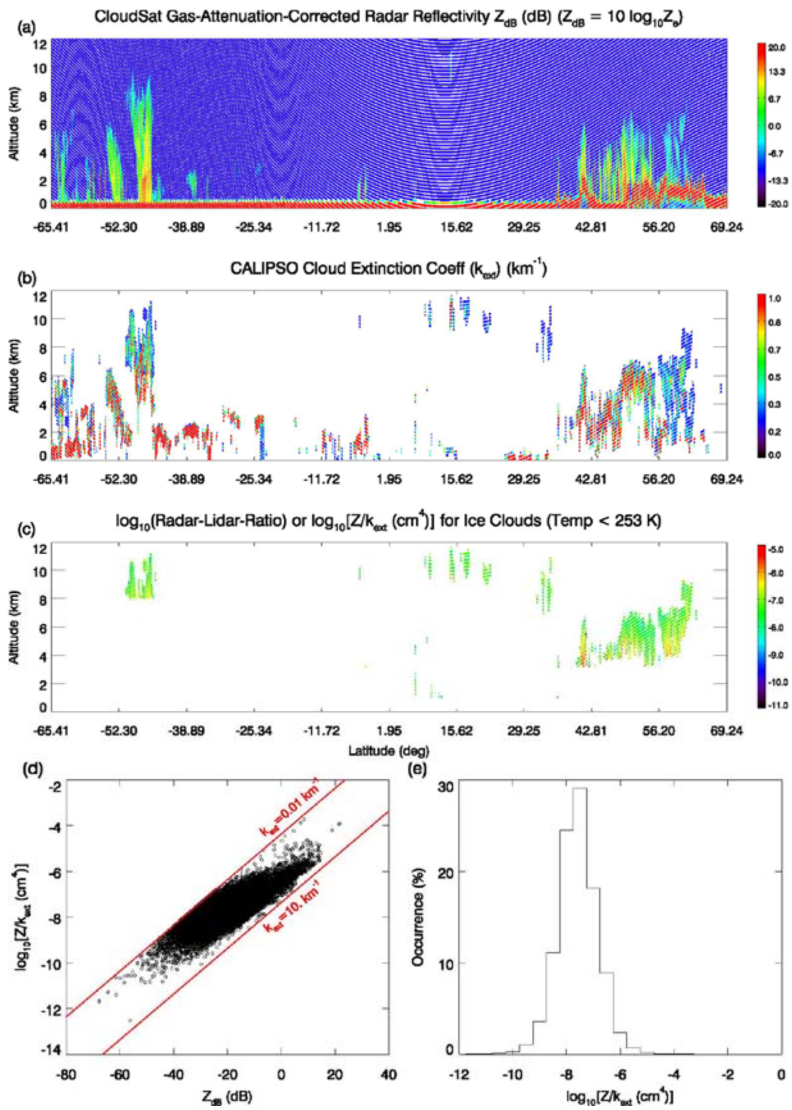


Figure 3. An example of $Z/k_{ext}$ from CloudSat CPR and CALIPSO CALIOP measurements on 3 March 2011 20 UTC. (a) Gas-atteunation-corrected radar reflectivity ($Z_{dB}$) (dB) from CloudSat 2B-GEOPROF product. Equivalent radar reflectivity ($Z_e$) in Eq. (8) is related to $Z_{dB}$ as $Z_{dB} = 10 \log Z_e$. (b) Cloud extinction coefficient $k_{ext}$ ($km^{-1}$) from CALIPSO CPRO product. (c) Distribution of $\log(Z/k_{ext})$ for ice clouds, where the ice clouds are defined for $k_{ext} > 0.01$ $km^{-1}$ and air temperature < 253 K. $Z$ in (c) is estimated from $Z_e$ using Eq. (9). (d) Scatter plot between $Z_{dB}$ and $\log(Z/k_{ext})$ for ice clouds. (e) Histogram of $Z/k_{ext}$ for ice clouds.

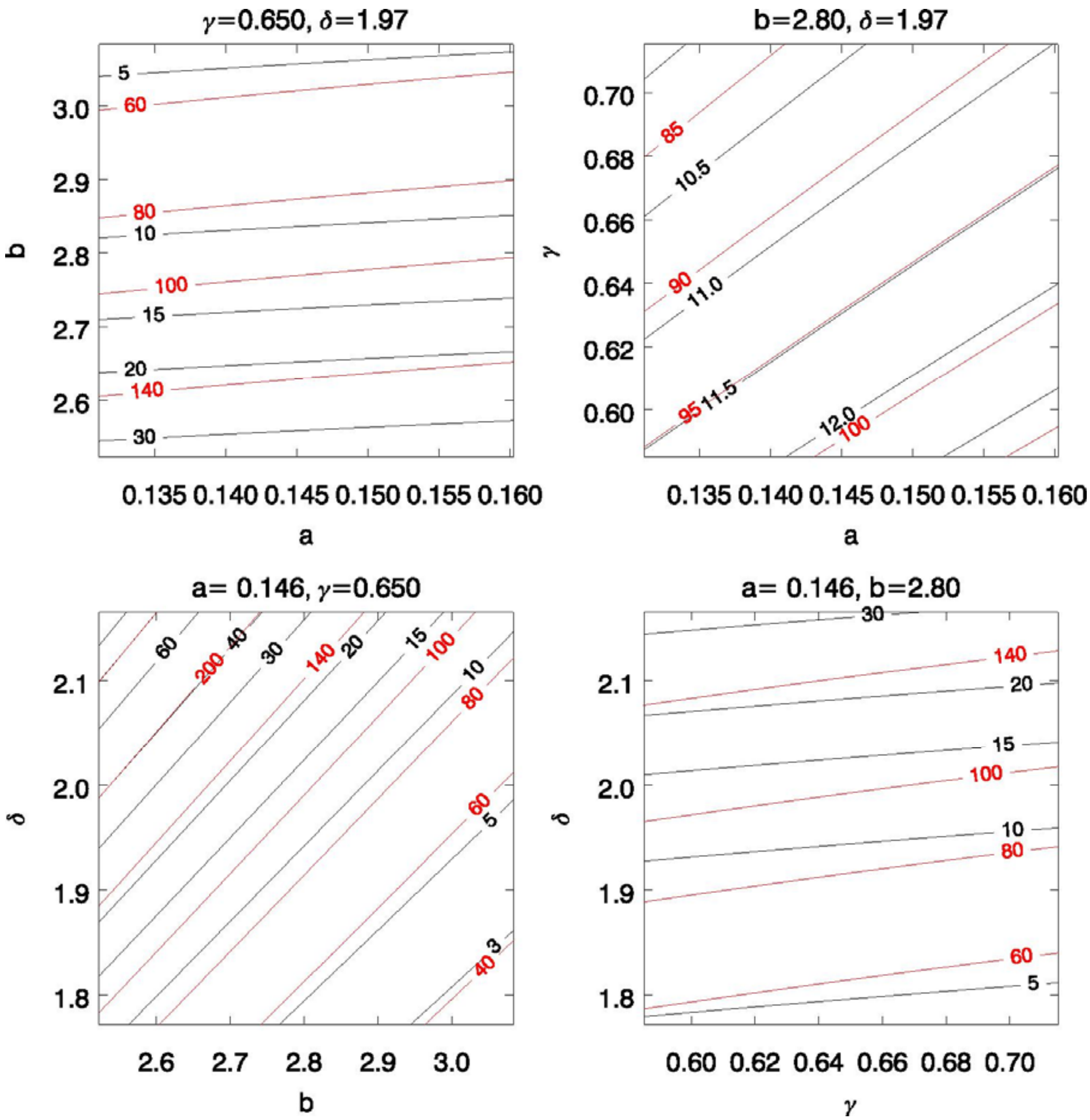


Figure 4. Retrieved $r_{eff}$ as a function of four parameters ($a$, $b$, $\gamma$, and $\delta$) expressing m-D and A-D relationships (Eqs. (1) and (2)). Reference values of $a$, $b$, $\gamma$, and $\delta$ are set using *Brown and Francis* for all $D$ (case (3) of Table 1). In each panel, two of four parameters ($a$, $b$, $\gamma$, and $\delta$) are perturbed by 10%. All panels use a gamma particle size distribution (PSD) with the dispersion factor ($\mu$) of −1. $Z/k_{ext}$ is set as $10^{-10}$ (black lines) and $10^{-6}$ cm$^4$ (red lines). $f_{Mie}$ is fixed as 1 for this figure but note that $f_{Mie}$ = 0.9 derives 1.5–3% larger $r_{eff}$ than those with $f_{Mie}$ = 1.

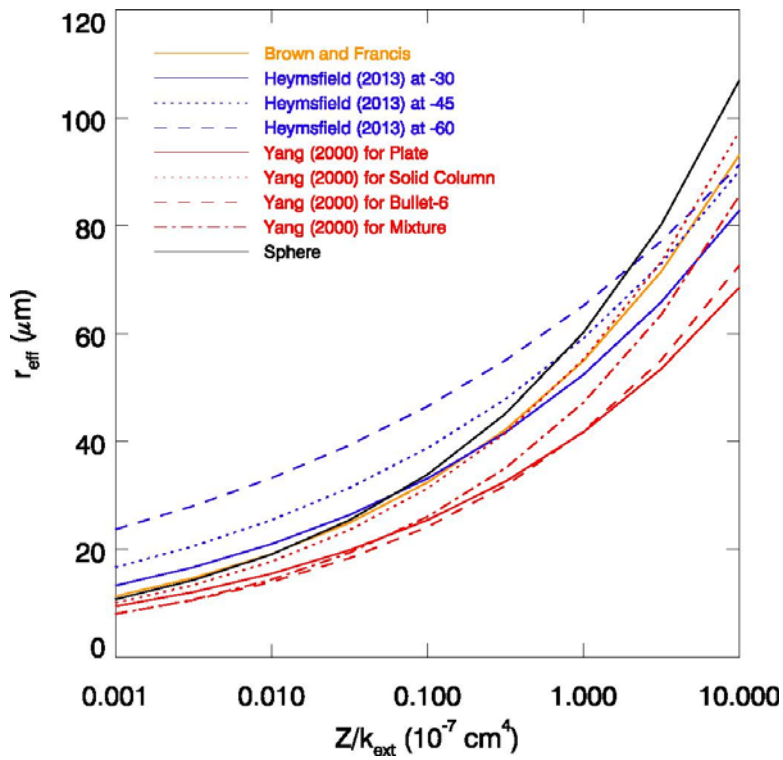


Figure 5. Retrieved $r_{eff}$ as a function of $Z/k_{ext}$ for nine sets of $a$, $b$, $\gamma$, and $\delta$ provided in cases (3)–(11) in Table 1. A gamma particle size distribution (PSD) is used with assuming dispersion parameter ($\mu$) as −1. $f_{Mie}$ is fixed as 1 for this figure but note that $f_{Mie}$ = 0.9 derives 1.5–3% larger $r_{eff}$ than those with $f_{Mie}$ = 1.

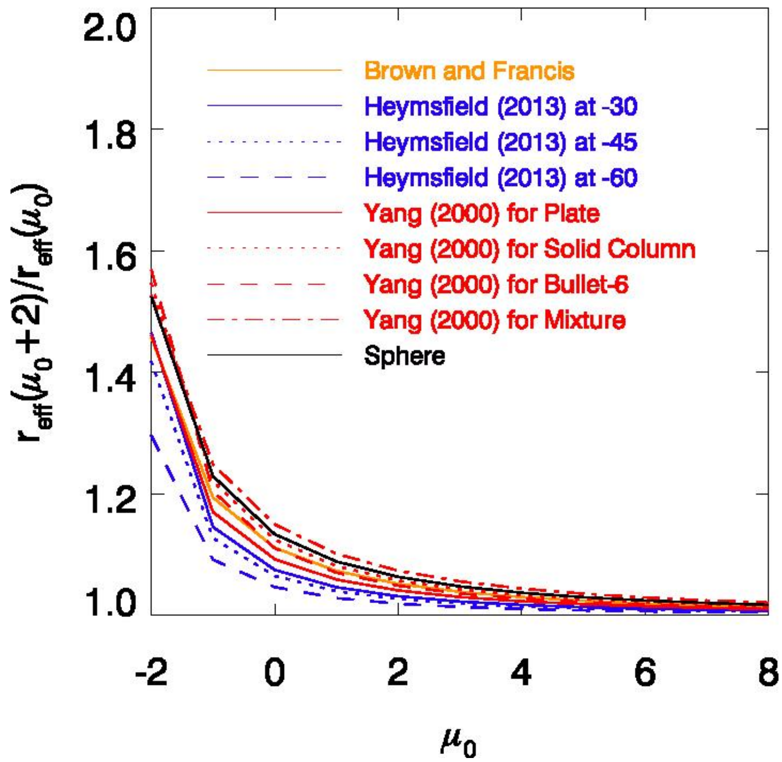


Figure 6. Ratio of $r_{eff}$ derived with $\mu = \mu_0+2$ to $r_{eff}$ derived with $\mu = \mu_0$, i.e. $r_{eff}(\mu_0+2)/r_{eff}(\mu_0)$. Different lines represent nine sets of $a$, $b$, $\gamma$, and $\delta$ provided by cases (3)–(11) of Table 1. $Z/k_{ext}$ is fixed as $10^{-7}$ cm$^4$. Note that $f_{Mie}$ does not change $r_{eff}(\mu_0+2)/r_{eff}(\mu_0)$, and thus is fixed as 1.

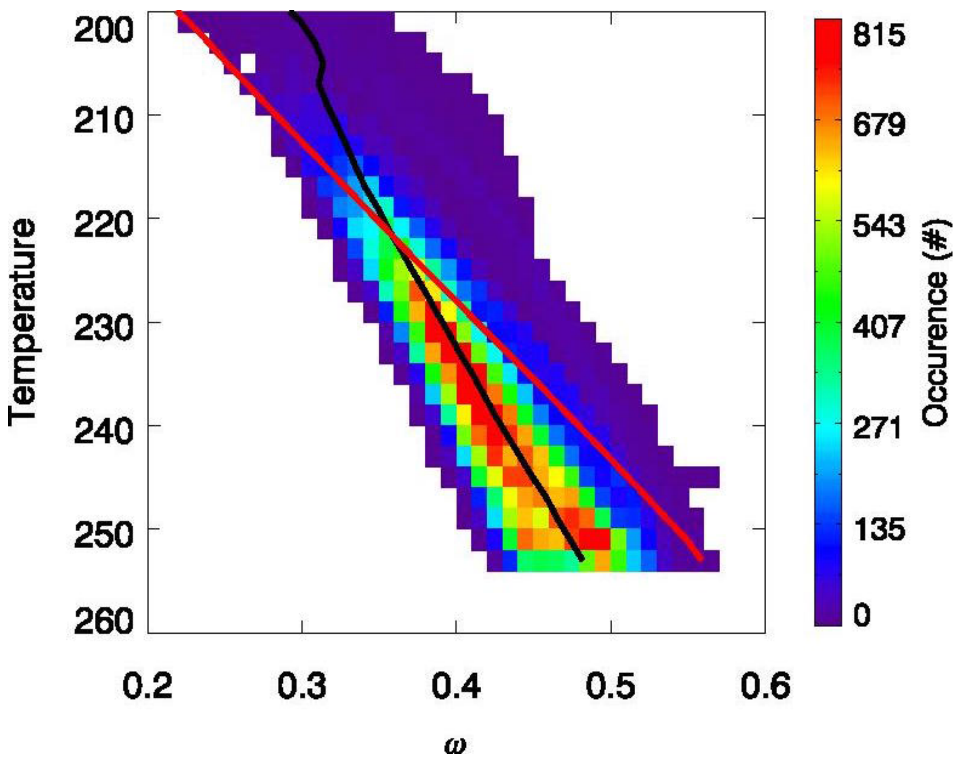


Figure 7. *A priori* $\omega$ (red solid line) and retrieved $\omega$ (frequency in color and average in black line) as a function of temperature from CloudSat 2B-CWC RO R04_E04 products. One track of CloudSat 2B-CWC RO data observed on 2 October 2008 19:00 UTC is used.

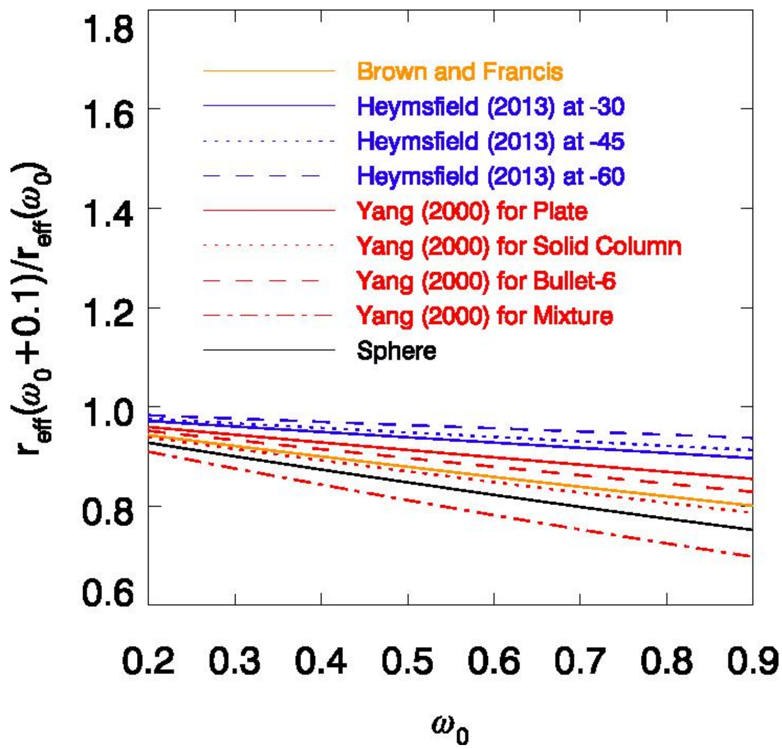


Figure 8. Ratio of $r_{eff}$ derived with $\omega = \omega_0+1$ to $r_{eff}$ derived with $\omega = \omega_0$, i.e. $r_{eff}(\omega_0 + 0.1)/r_{eff}(\omega_0)$. Different lines represent nine sets of $a$, $b$, $\gamma$, and $\delta$ provided in cases (3)–(11) of Table 1. $Z/k_{ext}$ is fixed as $10^{-7}$ cm$^4$. Note that $f_{Mie}$ does not change $r_{eff}(\omega_0 + 0.1)/r_{eff}(\omega_0)$, and thus is fixed as 1.

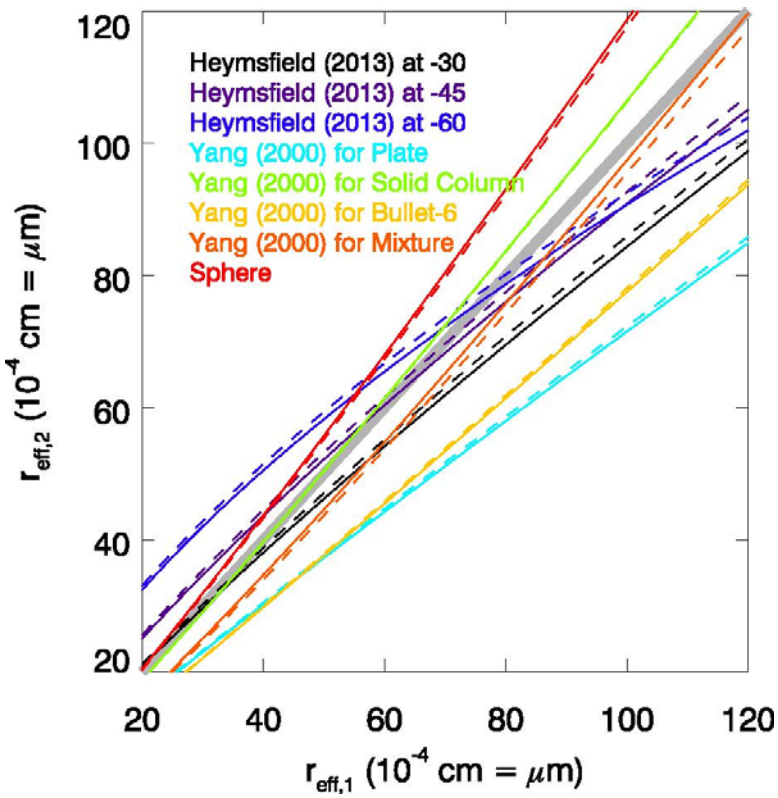


Figure 9. Relationships between $r_{eff,1}$ and $r_{eff,2}$. $r_{eff,1}$ is the effective radius retrieved with $a$, $b$, $\gamma$, and $\delta$ of *Brown and Francis* for all $D$ (case (3) of Table 1), and $r_{eff,2}$ is the effective radius retrieved from other sets of $a$, $b$, $\gamma$, and $\delta$ in cases (4)–(11) of Table 1. Both $r_{eff,1}$ and $r_{eff,2}$ are retrieved using the same gamma particle size distribution (PSD). Two values of $\mu$ are considered at $T = -75$°C (solid line) and $-5$°C (dashed line) using Eq. (31). It is assumed that two algorithms use the same Mie correction factor ($f_{Mie,1} = f_{Mie,2}$). Grey solid line indicates the one-to-one line.

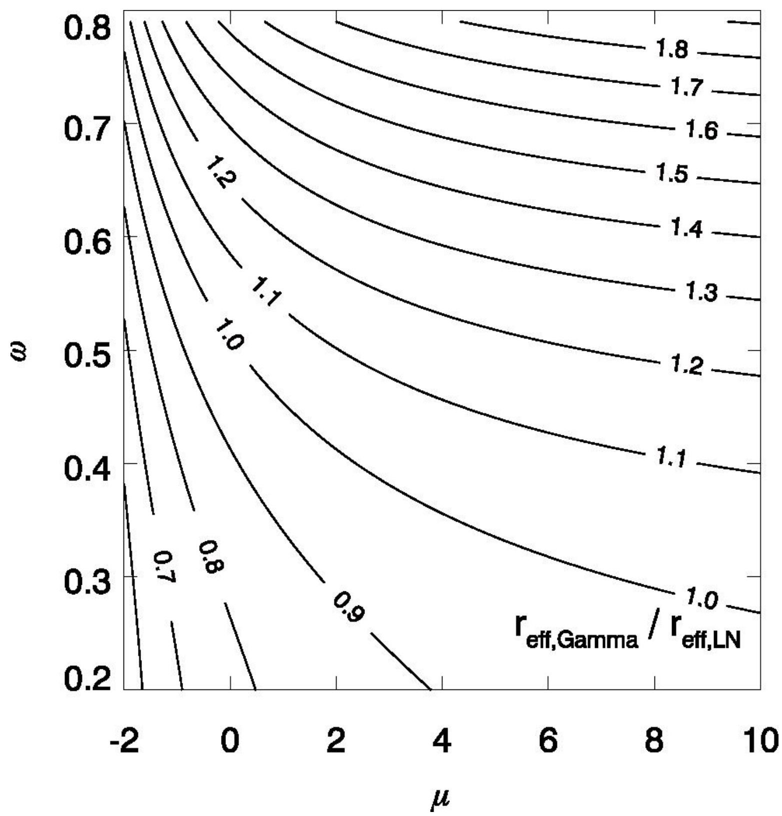


Figure 10. The ratio of $r_{eff,Gam}$ to $r_{eff,LN}$, where $r_{eff,Gam}$ is an effective radius retrieved from a gamma PSD and $r_{eff,LN}$ is an effective radius retrieved from a lognormal PSD. The ratio is provided as a function of dispersion ($\mu$) of the gamma particle size distribution (PSD) and width parameter ($\omega$) of the lognormal PSD. Both $r_{eff,Gam}$ and $r_{eff,LN}$ use the same $a$, $b$, $\gamma$, and $\delta$ from *Brown and Francis* for all $D$ (case (3) of Table 1). It is assumed that two algorithms use the same Mie correction factor ($f_{Mie,Gam} = f_{Mie,LN}$).

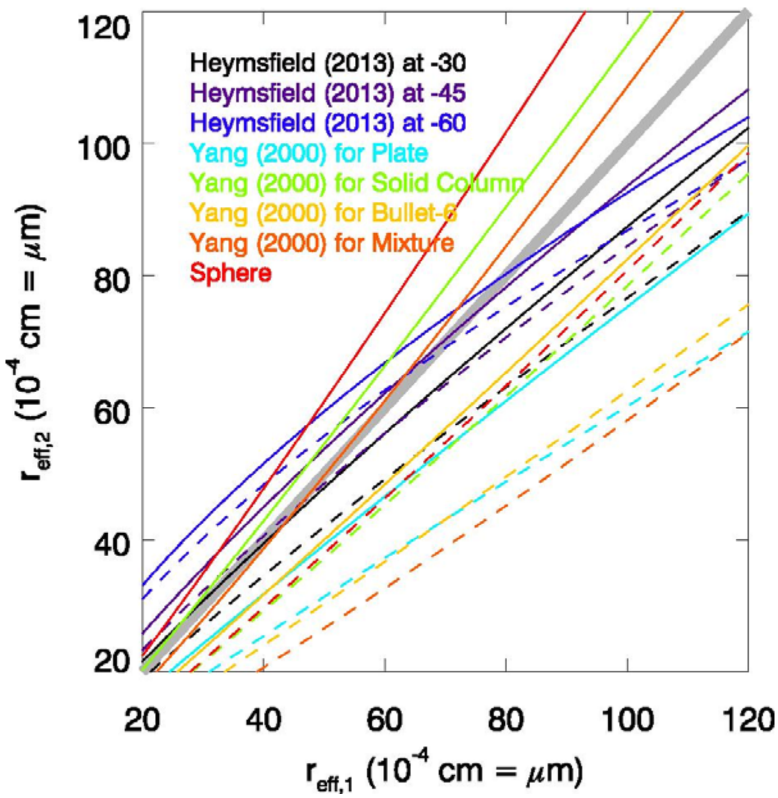


Figure 11. Same as Fig. 9 except that $r_{eff,2}$ uses a lognormal particle size distribution (PSD) instead of a gamma PSD. $\mu$ of the gamma PSD is computed with Eq. (31), and $\omega$ of the lognormal PSD is computed with Eq. (47) for temperatures at −75°C (solid lines) and −5°C (dashed lines). It is assumed that two algorithms use the same Mie correction factor ($f_{Mie,1} = f_{Mie,2}$).

Table A1. A magnitude of each term of Eq. (A10) with the minimum of ($\mu + \delta + 1$) as ($\delta - 1$).

| Source of $a$, $b$, $\gamma$, and $\delta$ | | (1) $(\mu_{min}+\delta+1)$ | (2) $f_0$ | (3) $f_1/(\mu_{min}+\delta+1)$ | (4) $f_2/(\mu_{min}+\delta+1)^2$ | (5) $f_3/(\mu_{min}+\delta+1)^3$ | {(1)+(2)} ÷ {total sum of Eq. (A10) × 100% |
|---|---|---|---|---|---|---|---|
| Brown and Francis (1995) and Francis et al. (1998) | All $D$ | 0.96859 | –0.08285 | 0.01307 | 0.00118 | –0.00153 | 98.6% |
| Heymsfield et al. (2013) | $T = -30$°C | 0.61407 | –0.23304 | 0.04851 | 0.01841 | –0.01086 | 87.8% |
| | $T = -45$°C | 0.60273 | –0.26787 | 0.05423 | 0.02410 | –0.01056 | 84.4% |
| | $T = -60$°C | 0.64494 | –0.32947 | 0.05709 | 0.02917 | –0.00540 | 81.6% |
| Yang et al. (2000) | Plate | 0.77561 | –0.16327 | 0.02936 | 0.00618 | –0.00502 | 95.3% |
| | Solid Column | 0.86699 | –0.04494 | 0.00825 | 0.00043 | –0.00118 | 99.1% |
| | Bullet-6 | 0.71808 | –0.10580 | 0.02196 | 0.00324 | –0.00465 | 96.6% |
| | Mixture | 1.46750 | 0.07443 | –0.01162 | 0.00075 | 0.00068 | 100.9% |
| Sphere | | 1.00000 | 0.00000 | 0.00000 | 0.00000 | 0.00000 | 100.0% |

Table A2. A magnitude of each term of Eq. (A20) with the minimum of ($\mu + \delta + 1$) as ($\delta - 1$).

| Source of $a$, $b$, $\gamma$, and $\delta$ | | (1) ($\mu_{min}+\delta+1$) | (2) $f_0$ | (3) $f_1/(\mu_{min}+\delta+1)$ | (4) $f_2/(\mu_{min}+\delta+1)^2$ | (5) $f_3/(\mu_{min}+\delta+1)^3$ | {(1)+(2)} ÷ {total sum of (A20)} × 100% |
|---|---|---|---|---|---|---|---|
| Brown and Francis (1995) and Francis et al. (1998) | All $D$ | 0.96859 | 1.31860 | –0.52608 | 0.71619 | –1.29037 | 112.4% |
| Heymsfield et al. (2013) | $T = -30°C$ | 0.61407 | 0.84097 | –0.42020 | 0.57546 | –1.05045 | 116.1% |
| | $T = -45°C$ | 0.60273 | 0.76564 | –0.37381 | 0.47484 | –0.80166 | 115.6% |
| | $T = -60°C$ | 0.64494 | 0.66353 | –0.28525 | 0.29347 | –0.39736 | 113.3% |
| Yang et al. (2000) | Plate | 0.77561 | 1.06130 | –0.47007 | 0.64320 | –1.17342 | 114.0% |
| | Solid Column | 0.86699 | 1.34362 | –0.60534 | 0.93713 | –1.92279 | 114.1% |
| | Bullet-6 | 0.71809 | 1.14745 | –0.57191 | 0.91387 | –1.94153 | 115.9% |
| | Mixture | 1.14675 | 1.72223 | –0.68140 | 1.02335 | –2.01143 | 112.2% |
| Sphere | | 1.00000 | 1.50000 | –0.62500 | 0.93750 | –1.85156 | 113.1% |

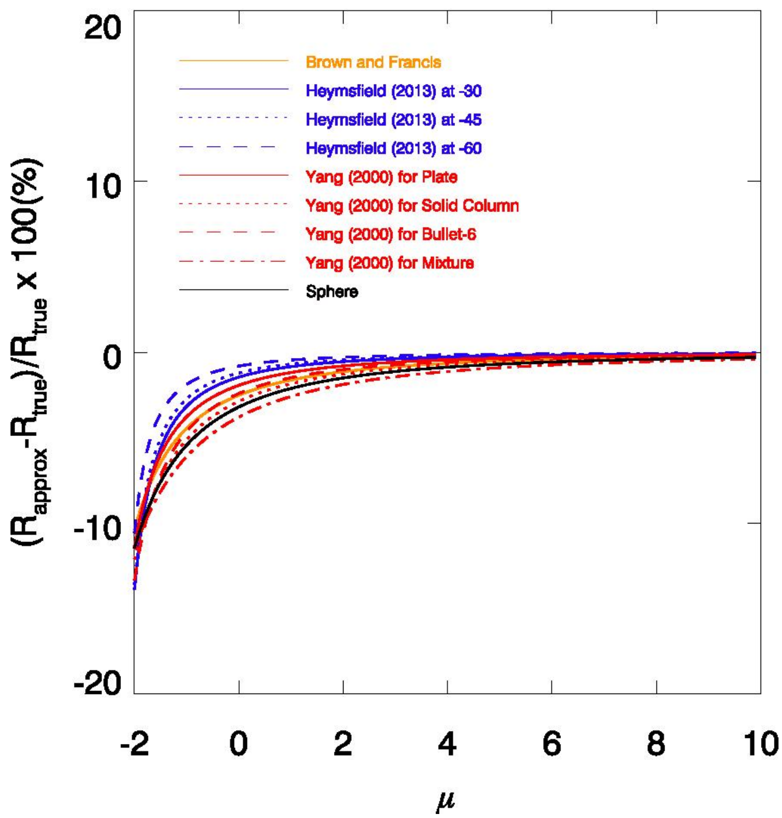


Figure A1. Errors of $R_{approx}$ relative to $R_{true}$ as a function of the dispersion factor ($\mu$) of a gamma particle size distribution (PSD). $R_{approx}$ is from Eq. (A23) and $R_{true}$ is from Eq. (A22). Different lines represent different sets of $a$, $b$, $\gamma$, and $\delta$ listed in Table 1 (cases (3)–(11)).

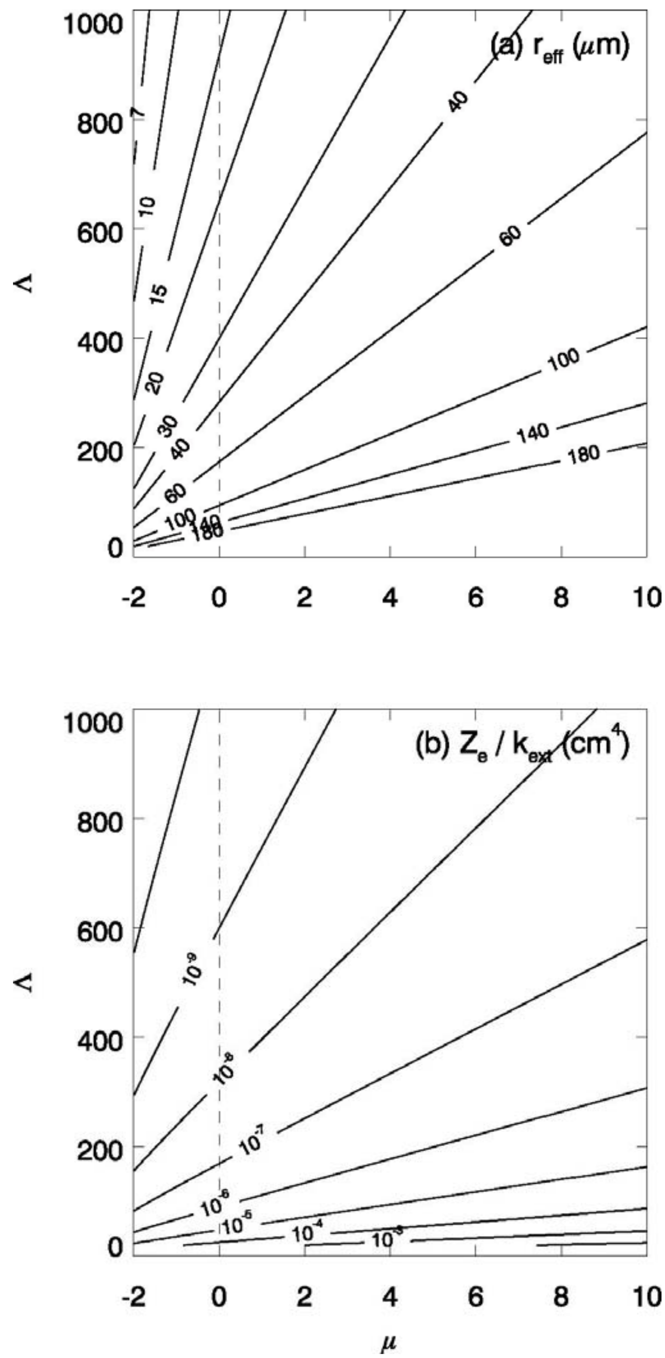


Figure B1. The contour of constant values of (a) $r_{eff}$ and (b) $Z/k_{ext}$ in a $\mu$-$\Lambda$ domain. $\mu$ is a dispersion and $\Lambda$ is a slope factor in a gamma particle size distribution (PSD) (Eq. 14). Equations (20) and (21) are used to compute $r_{eff}$ and $Z/k_{ext}$, respectively. The particle shape of *Brown and Francis* for all $D$ (case (3) of Table 1) is used for $a$, $b$, $\gamma$, and $\delta$.